Raman Spectroscopy of the Iron Oxides in the Form of Minerals, Particles and Nanoparticles

Raman Spectroscopy of the Iron Oxides in the Form of Minerals, Particles and Nanoparticles

Amelia Carolina Sparavigna

Department of Applied Science and Technology, Polytechnic University of Turin, Italy

Email: amelia.sparavigna@polito.it

Abstract

Magnetic iron oxides, such as Fe_3O_4, α-Fe_2O_3, γ-Fe_2O_3, have unique magnetic, catalytic and biochemical features, rendering them suitable for several specific technological and biomedical applications. In a previous study, for instance, we considered the magnetite Fe_3O_4 nanoparticles dispersed in supporting materials to obtain composites that can better respond to electromagnetic interferences with an increased EMI shielding effectiveness. Here we investigate how to distinguish the iron oxide nanoparticles by means of their Raman spectra. We will stress that literature is evidencing a challenge. This challenge is due to the fast transformations of iron oxides when laser power is applied. Therefore, the Raman spectroscopy needs to be considered carefully for determining the nature of the iron oxide present in the investigated samples. The role of oxidation of magnetite will be addressed in detail. In the review, the reader can find the Raman "fingerprints" of some oxides such as Magnetite, Maghemite, Hematite, Goethite, Lepidocrocite, Akaganeite and Siderite, when considered as minerals or nanoparticles. Moreover, we will also discuss some Raman spectra of iron oxides in composites and other materials (encapsulated iron oxides, biochar decoration, red mud). The fitting of some Raman spectra obtained by means of the q-Gaussian Tsallis functions is also shown.

Keywords: Raman spectroscopy, Magnetic iron oxide nanoparticles, Fe_3O_4, Magnetite, Hematite, Maghemite, Electromagnetic interference shielding effectiveness, IONPs, Biochar, Red mud

Torino, September 11, 2023. https://doi.org/10.26434/chemrxiv-2023-22kh4-v2

Introduction

In a previous study (Sparavigna, 2023), we considered the iron oxide Fe_3O_4 nanoparticles and their dispersion in a supporting material, to obtain a composite which can better respond to the electromagnetic (EM) fields by absorbing a part of their energy. The use of magnetic nanoparticles (NPs) aims to improve the EM interference shielding effectiveness (EMI-SE) of the composites and, at the same time, to reduce their reflection loss (RL) (Avloni et al., 2007). The iron oxide nanoparticles are sometimes mentioned as being MIONs (Monocrystalline Iron Oxide Nanoparticles) or designed as belonging to the family of IONPs, iron oxide NPs. Because of their superparamagnetic (SPM) behavior, the Fe_3O_4 particles are SPM IONPs or SPIONs (Wallyn et al., 2019). Dispersed in a supporting material, IONPs can respond to an external magnetic field (Tong et al., 2019).

About IONPs, a review was proposed by Wu et al., 2015. The review illustrates the "strategies in the preparation, microstructure, and magnetic properties of bare and surface functionalized" IONPs (Wu et

al., 2015). Biological applications are addressed in the review starting from the magnetic IONPs used "as a contrast agent for in vitro diagnostics", in methods "practiced for nearly half a century" (Wu et al. and references therein). More recently, magnetic IONPs has been largely investigated for the targeted drug delivery and magnetic resonance imaging (MRI), besides other biological applications (see Wu et al. and references therein). Among the technological applications, we focused on the EMI-SE increase obtained by means of Fe_3O_4 nanoparticles, but catalysis is also largely employing them (reviews by Pereira et al., 2012, Pouran et al., 2014, and Kumar et al., 2022).

Wu et al., mentioning Cornell and Schwertmann, 2003, tell that eight iron oxides are known, and that the most popular are hematite (α-Fe_2O_3), magnetite (Fe_3O_4) and maghemite (γ-Fe_2O_3), which are possessing "polymorphism, involving temperature-induced phase transition". "Each of these three iron oxides has unique biochemical, magnetic, catalytic, and other properties which provide suitability for specific technical and biomedical applications" (Wu et al., 2015). The set of the eight oxides is made of the Fe^{II} oxide (FeO, iron(II) oxide, wüstite), the mixed oxides of Fe^{II} and Fe^{III}, among which we have Fe_3O_4, Iron(II,III) oxide, that is the magnetite, and of the oxide of Fe^{III}, Fe_2O_3, in the form of hematite, maghemite and other phases. Besides oxides, we have hydroxides and oxyhydroxides. "All together, there are sixteen known iron oxides and oxyhydroxides with different mineral structures" (Fernández-Remolar, 2015). Let us stress that Fe_3O_4 (magnetite) is $Fe^{II}Fe_2^{III}O_4$, containing the divalent form of iron (Fernández-Remolar, 2015). Cornell and Schwertmann, 2003, are calling all these sixteen chemical compounds as "iron oxides". We will do the same.

Having so many oxides, we can ask ourselves if it is possible to distinguish them by means of the Raman spectroscopy. This spectroscopy is named after the Indian physicist Sir Chandrasekhara Venkata Raman. The technique is based on the vibrational modes of molecules, relying upon the inelastic scattering of photons, that is the Raman scattering. A source of monochromatic light, usually a laser, is providing the photons interacting with molecular vibrations, phonons and other excitations. The outcoming inelastically scattered photons have a shifted frequency, which is giving information about the vibrational modes. The elastically scattered photons, which have a wavelength corresponding to the laser line (Rayleigh scattering), are filtered out. The several iron oxides possess different crystal lattices and symmetries, so phonons and other vibrational modes seem being quite distinguishable, and consequently the Raman spectroscopy appears as a method easy to handle.

As stressed by Monika Hanesch, 2009, in her study about the Raman spectroscopy of synthetic and natural iron oxides and (oxy)hydroxides, "most of them can be identified by magnetic methods, but there are some minerals that are not easy to differentiate from each other. In these cases, the magnetic methods can be complemented by Raman spectroscopy" (Hanesch, 2009). However, Raman spectroscopy must be carefully used: "A major challenge is the fast transformation of many iron minerals if laser power is applied, especially if the material is poorly crystallized as often is the case in environmental material" (Hanesch, 2009). Monika Hanesch used very low laser powers. But, even with low powers, "the investigated iron minerals could be distinguished from each other."

Let us start our review showing some Raman spectra from RRUFF and ROD databases. References to RRUFF and ROD databases are Lafuente et al., 2015, and El Mendili et al., 2019, respectively.

ROD (Raman Open) database

In this database, we can find spectra of Magnetite and Hematite. The iron(II,III) oxide is the chemical compound with formula Fe_3O_4. The mineral form is the magnetite. The iron(III) oxide (Fe_2O_3) occurs as the mineral hematite.

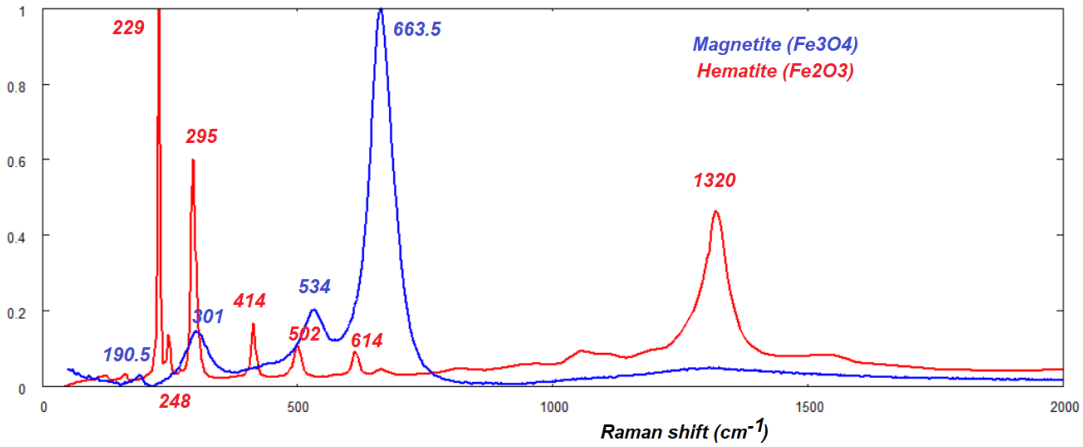

Fig.1: Raman spectra of Fe_3O_4 (Magnetite, laser 633 nm) and Fe_2O_3 (Hematite, laser 514 nm). Fe_3O_4 (data courtesy Kumar et al., 2019), https://solsa.crystallography.net/rod/3500283.rod, Fe_2O_3 (data courtesy El Mendili et al., 2012), https://solsa.crystallography.net/rod/1000001.rod

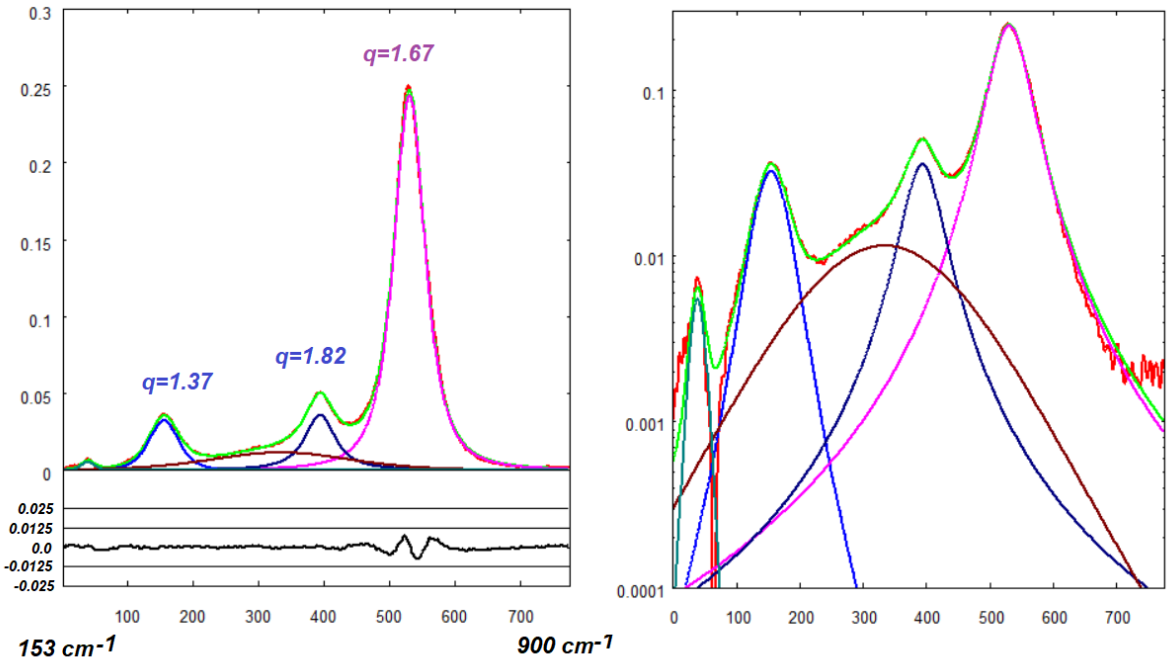

Fig.2a: Deconvolution of a part of the Magnetite spectrum obtained by means of q-Gaussian functions (see Appendix A). The best fit (green) is onto processed data (red) provided by Kumar et al., 2019; frequency range is from 153 to 900 cm^{-1} (see Fig.1). For the deconvolution, five q-Gaussians have been used. For the stronger peaks the values of the q-parameters are given in the figure. A quite flat q-Gaussian seems being related to a band at 475 cm^{-1}. In the following discussion of the magnetite Raman spectrum, we will see that a band at 470-472 cm^{-1} has been detected (Hart et al., 1976). In the lower part of the plot, the misfit is also proposed. On the right, the same fit is shown with the log scale for y-axis (semi log scale). Data and q-Gaussians are given as functions of integers n (equally spaced points used in fitting), for the x-axis which is representing the Raman shift. A convenient scale is used for the y-axis (intensity axis). The fitting calculation is obtained by minimizing the sum of the squares of the deviations.

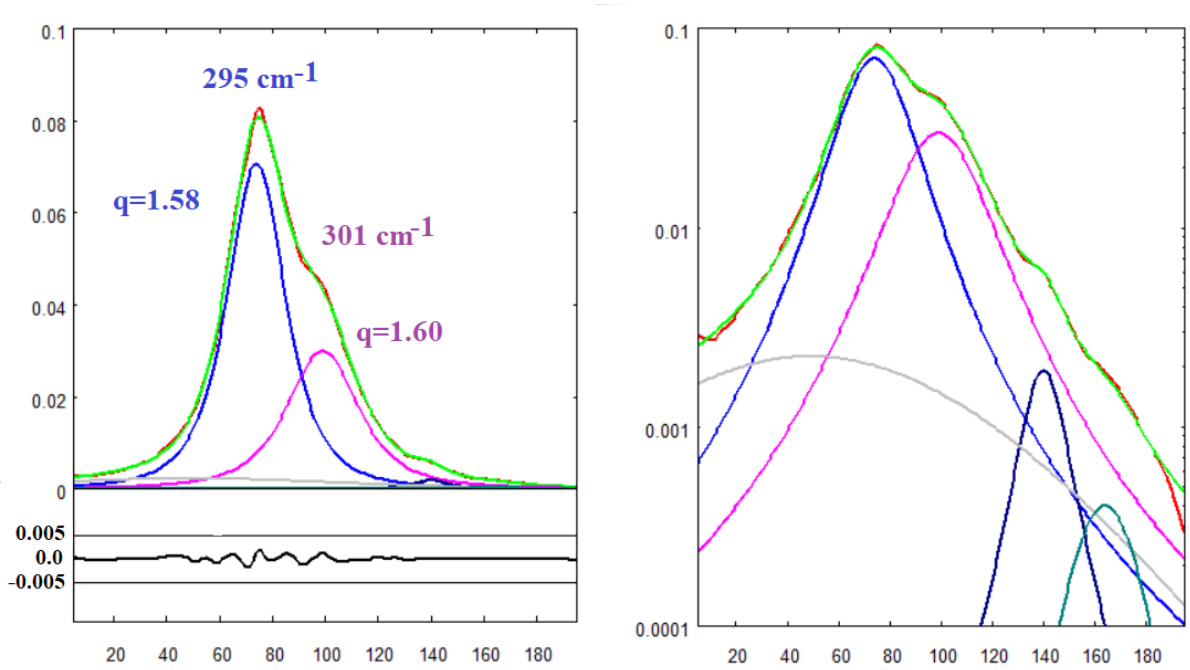

Fig.2b: Deconvolution with q-Gaussian functions of the Hematite peak at 295 cm^{-1} to evidence its shoulder. The best fit (green) is onto processed data (red) provided by El Mendili et al., 2012 (see Fig.1). For the deconvolution, five q-Gaussians have been used. For the peak and its shoulder, the values of the q-parameters are given in the figure. On the right, the same fit is shown with the log scale for y-axis (semi log scale). The fitting calculation is obtained by minimizing the sum of the squares of the deviations.

In the Figures 2a and b, we are also proposing the deconvolution in q-Gaussian (Tsallis) functions of a part of the magnetite and hematite spectra (see Appendix about q-Gaussians). The parameter q is spanning values from 1 to 2. For q=2, the q-Gaussian function is a Lorentzian distribution, for q close to 1, it is the Gaussian. The deconvolution in q-Gaussians of Raman and SERS spectra has been proposed for the first time by me (Sparavigna, 2023).

Raman shift (cm^{-1}), Hematite: 229 (strong) 248 295 414 502 614 1320 (strong)

Raman shift (cm^{-1}), Magnetite: 190.5 301 534 663.5 (strong)

RRUFF database

In RRUFF Project website, searching for **magnetite** ($Fe^{2+}Fe^{3+}{}_2O_4$), we can find the following Raman spectra (https://rruff.info/magnetite): R060191, source Lloyd Twaites, R060222, source Rock Currier, R060656, source Michael Scott, R061111, source Michael Scott, R080025, source William W. Pinch, and R140861, source Rock Currier.

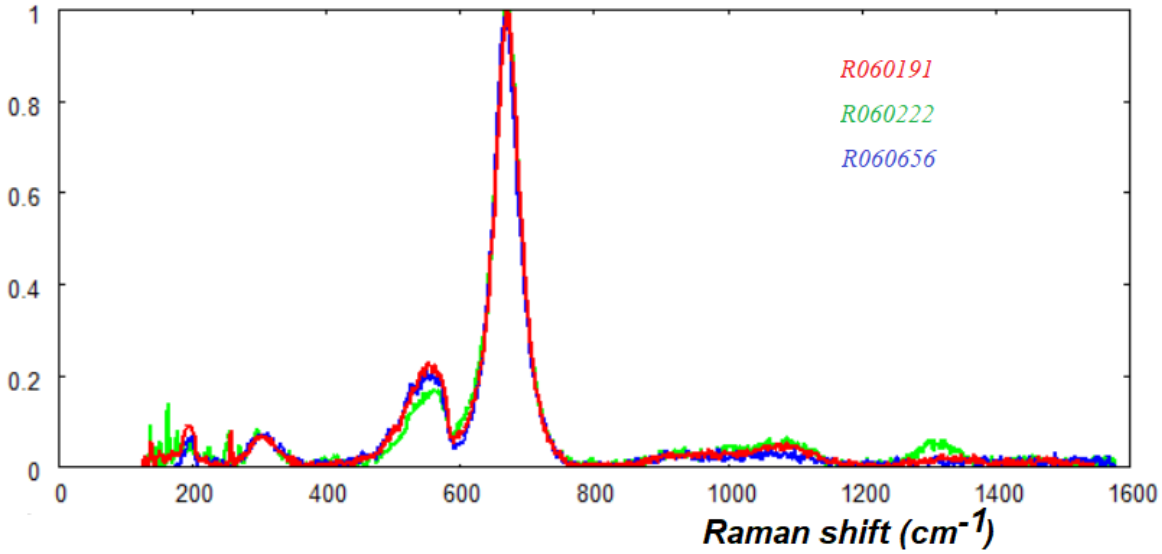

Fig.3a: Raman spectra from RRUFF Project website, R060191, R060222 and R060656 (Magnetite).

In the Figure 3a, the Raman spectra (depolarized) of R060191, measured chemistry $(Fe^{2+}_{0.97}Mg_{0.03})(Fe^{3+}_{0.97}Al_{0.03})_2O_4$, R060222 measured chemistry $(Fe^{2+}_{0.95}Mg_{0.05})(Fe^{3+}_{0.99}Al_{0.01})_2O_4$ and R060656 measured chemistry $(Fe^{2+}_{0.98}Mg_{0.01}Mn_{0.01})(Fe^{3+}_{1.96}Ti_{0.02}Mg_{0.02})O_4$ are shown.

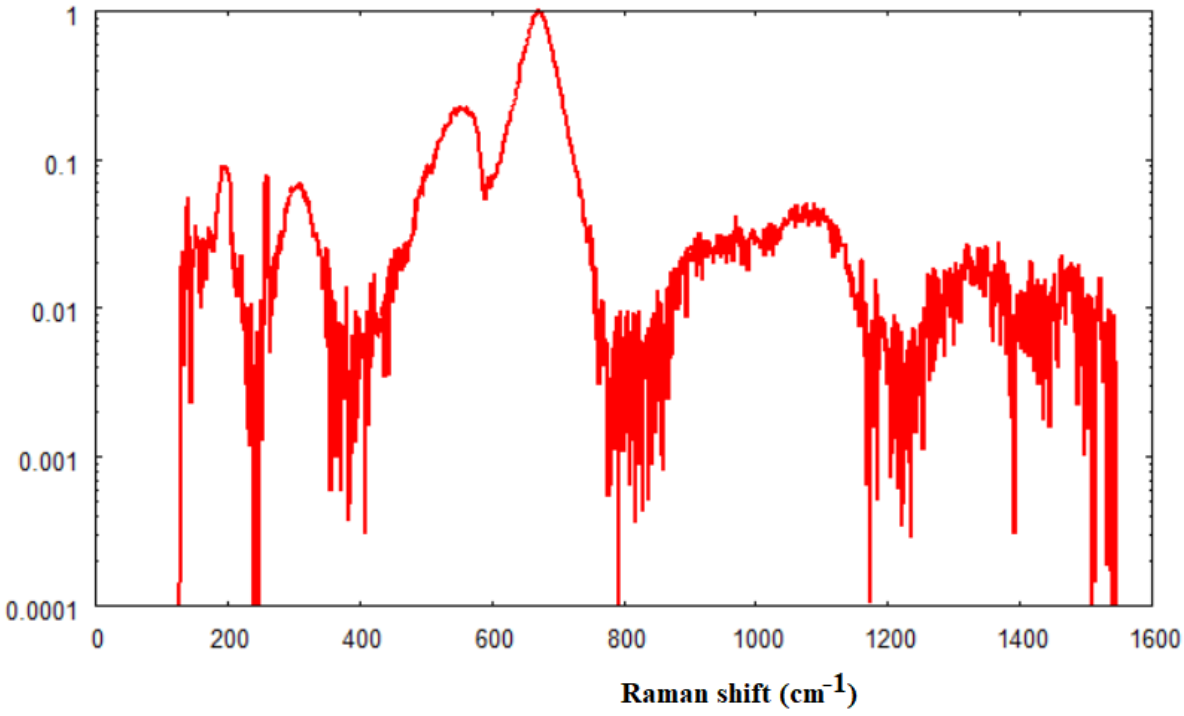

Fig.3b: Raman spectrum from RRUFF Project website, R060191, in semi logarithmic scale. About 500 cm^{-1}, the semi log scale is evidencing a possible band (shoulder).

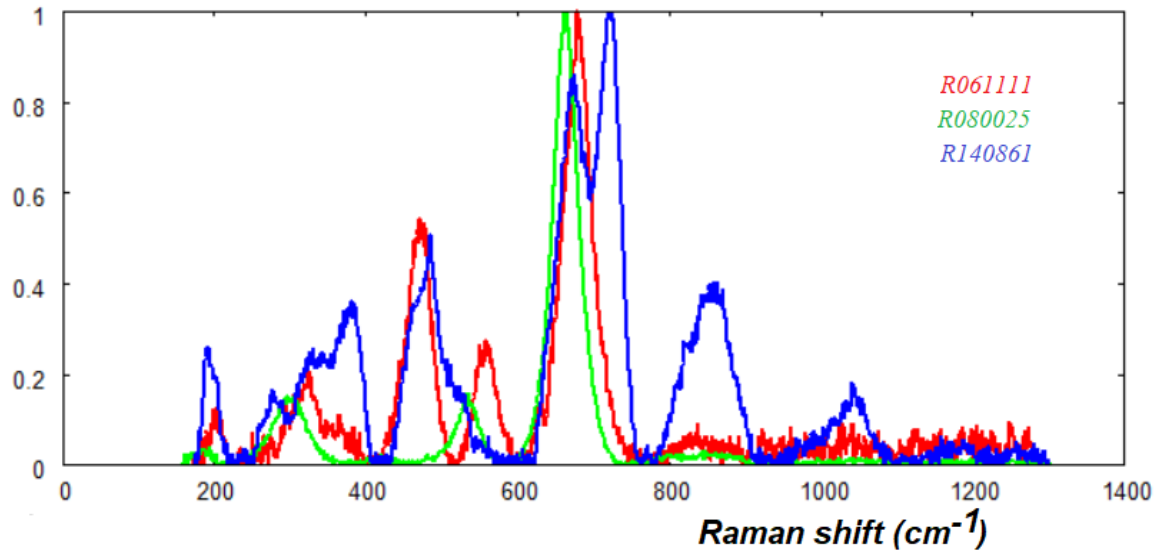

Fig3c: Raman spectra from RRUFF Project website, R061111, R080025 and R140861 (Magnetite).

In the Figure 3c, the Raman spectra (laser 532 nm) of R061111, according to RRUFF measured chemistry $(Fe^{2+}_{0.51}Ni_{0.48}Co_{0.01})_{\Sigma=1}Fe^{3+}_{2}O_4$, trace amounts of Al, R080025. no measured chemistry available, and R140861 measured chemistry $(Fe^{2+}_{0.82}Ni_{0.18})Fe^{3+}_{2.00}O$, are given. Note that we have a large presence of impurities, in particular in the third sample R080025.

Let us consider from RRUFF the **hematite samples** too, https://rruff.info/hematite , which are R040024 University of Arizona Mineral Museum, X050102 CIT – 2058, R050300 Eugene Schlepp, R060190 Lloyd Twaites, R070240 Michael Scott, and R110013 University of Arizona Mineral Museum.

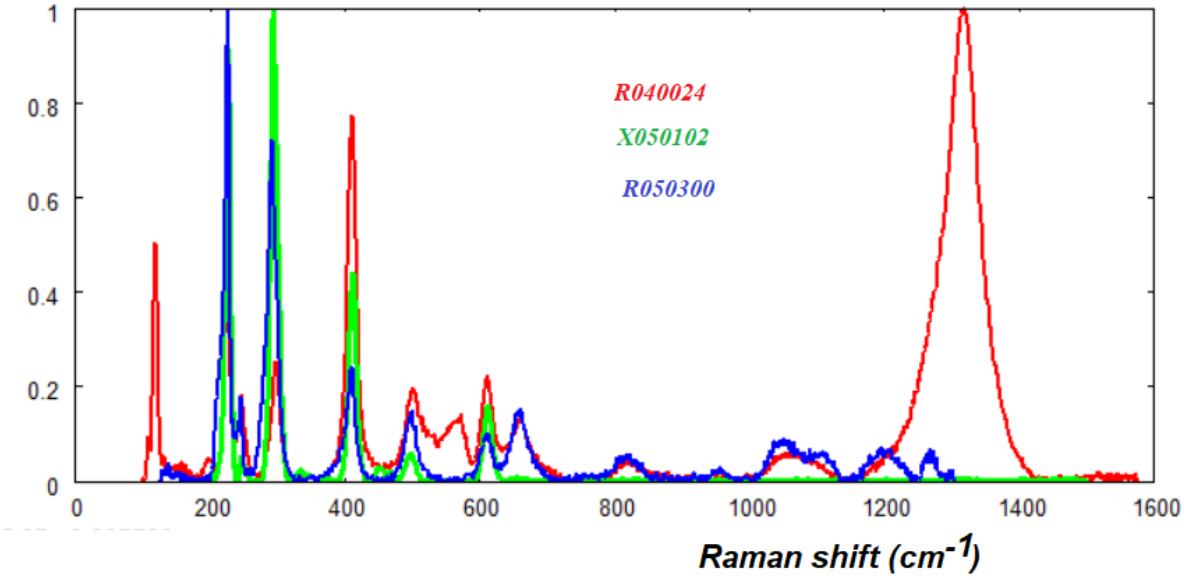

Fig.4a: Raman spectra from RRUFF Project website, R040024, X050102 and R050300 (Hematite).

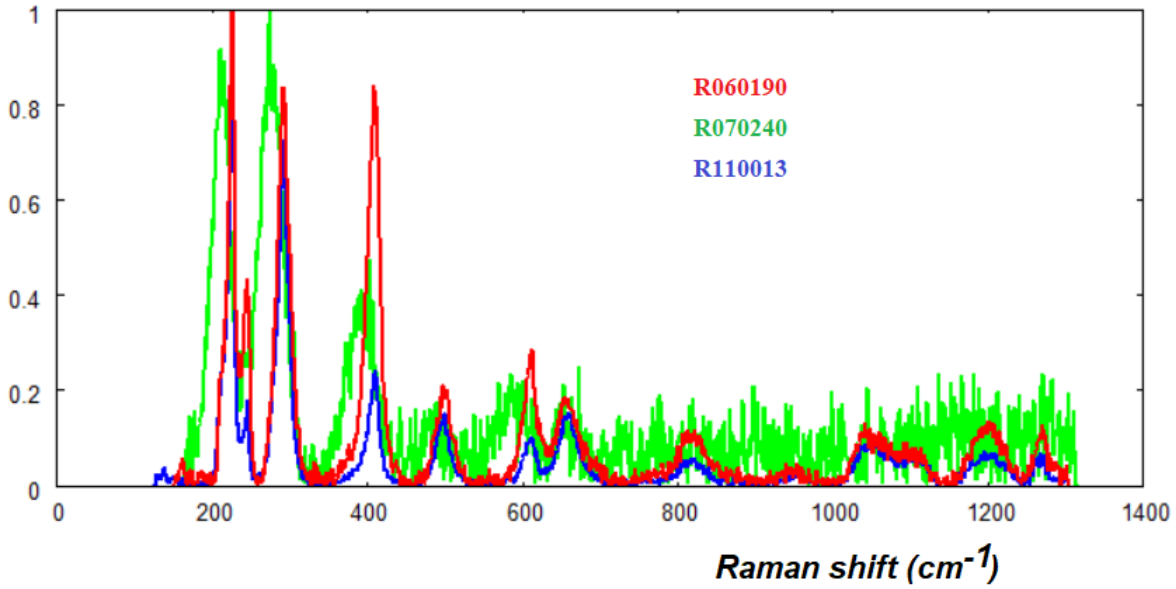

Fig.4b: Raman spectra from RRUFF Project website, R060190, R070240 and R110013 (Hematite).

In the Figure 4a we can see the Raman spectra from RRUFF Project website, R040024 $(Fe_{1.99}Al_{0.01})O_3$ depolarized, X050102 no chemistry data available, laser 785 nm, and R050300 $Fe_{2.00}O_3$. In the Figure 4b, we find R060190 laser 532nm, R070240 $Fe_{2.00}O_3$ laser 532nm, and R110013 Fe_2O_3 532 nm.

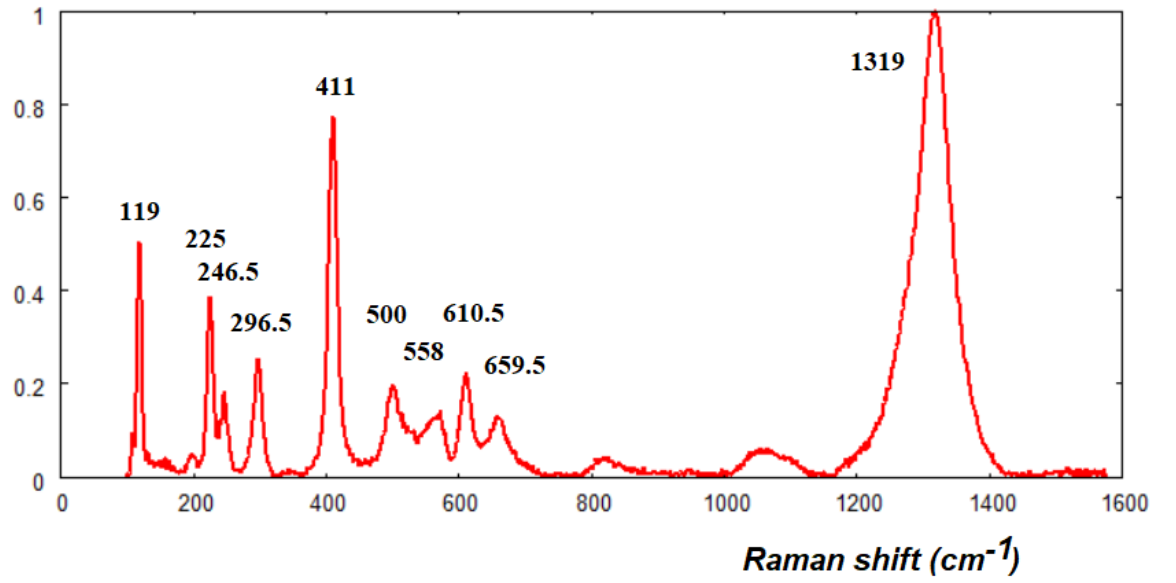

Fig.5: Raman spectrum R040024 (hematite) and positions of peaks.

Raman shift (cm^{-1}), Hematite ($(Fe_{1.99}Al_{0.01})O_3$):

119 225 246.5 296.5 411 (strong) 500 558 610.5 659.5 1319 (strong)

Magnetite and laser-induced thermal effects and oxidation

Let us consider the article entitled "Raman study of magnetite (Fe_3O_4): laser-induced thermal effects and oxidation", by Shebanova and Lazor, 2003. In it, we can find a study of natural magnetite (single crystal and powder) with the Raman spectroscopy at different laser powers. The laser power, if enough high, is inducing the oxidation of the sample (in the Appendix B, the phenomenon of the laser induced bandshift is illustrated for graphite). "In the course of the oxidation of the single crystal of magnetite, the first characteristic features of hematite appear at about 300 and 410 cm^{-1}, at a temperature close to 240 °C. This may explain the *erroneous assignment* of these modes to the intrinsic Raman modes of magnetite in some studies" (Shebanova & Lazor, 2003). In the case of a finely powdered magnetite, we have a material which is "much more easily prone to oxidation". During the reaction mechanism, we find the "metastable maghemite (γ-Fe_2O_3) before the final product hematite is formed".

Mentioning De Faria et al., 1997, Shebanova and Lazor stress that "the high density of power from a laser excitation source often poses a problem in a Raman experiment owing to its adverse effects on a sample". In the case of *micro-Raman* experiments, where the laser beam is focused to a spot of a few micrometers in diameter, the spot temperature can increase even by hundreds of degrees. Consequently, the shift of Raman modes changes. But we can have also "the alteration of a sample as the result of effects such as oxidation, recrystallization, order–disorder transitions (cation redistribution), phase transition or decomposition" (Shebanova & Lazor, 2003). The iron oxides are "good absorbers" of laser radiation, and therefore "belong to materials where *care has to be taken* when conducting a Raman experiment". Moreover, magnetite is easily oxidized at elevated temperatures, when measurements are made "in open air containing moisture" (Shebanova & Lazor, 2003).

In the Figure 2 of the article by Shebanova and Lazor we can see Raman spectra of a single crystal of magnetite, obtained in the case of a stepwise increase in laser power. As in the case of our Figure 1, for the laser power of 10 mW, we can observe the peaks at 190.5 (very weak), 301 (weak), 534 and 663.5 (strong) (cm^{-1}). "New features in the spectra begin to appear when the power is increased above 20 mW. … Concurrently, the intensities of the Raman bands of magnetite gradually vanish. Analysis of the spectrum of the final reaction product shows that magnetite, subjected to increased laser power in the course of the Raman experiment conducted in air, was oxidized to the trivalent iron oxide hematite (α-Fe_2O_3)" (Shebanova & Lazor, 2003).

Shebanova and Lazor made also experiments on fine-grained powder of magnetite. The increase of laser power is producing effects on Raman spectrum attributed to oxidation. "Broadening and a deterioration of bands in the 400–600 cm^{-1} region, along with the development of a new peak at about 700 cm^{-1}, indicate the first stage of the oxidation of magnetite … The presence of hematite bands in the spectrum, along with those of maghemite, is explained by the *metastability of maghemite* with respect to hematite. The Raman spectra collected at higher powers are consistent with pure hematite" (Shebanova & Lazor, 2003).

Magnetite Raman shift frequencies

In the article entitled "Raman spectroscopic study of magnetite ($FeFe_2O_4$): a new assignment for the vibrational spectrum", by the same authors, Shebanova and Lazor, 2003, we can find an overview of Raman frequencies available from different studies.

The following Raman shift frequencies are given in cm^{-1}.

Verble (1974), at 77K:	*300*	*320*	*420*		*560*		*680*			
Boucherit et al. (1991):					*550*		*670*			
Hart et al. (1976):	*298*	*320*	*420*	*472*	*550*		*676*			
Dünnwald and Otto (1989):	*298*	*319*	*418*	*470*	*550*		*676*			*1322*
Ohtsuka et al. (1986):					*540*		*665*			
Thierry et al. (1991):					*550*		*670*			
De Faria et al. (1997):	*301.6*				*533.6*		*662.7*			
Gasparov et al. (2000)*:*	*193*	*308*			*540*		*670*			
Degiorgi et al. (1987) at 130K:	*160*		*318*	*410*	*462*	*542*		*672*		
Graves et al. (1988):	*226*		*336*		*490*	*570*		*706*		
Li et al. (2000):		*311*				*540*		*665*		
Bersani et al. (1999):		*311*				*541*		*666*		
Murugappan et al. (2014):		*311*	*360*		*488*			*677*		
Gupta et al. (2002):		*300*		*410*		*540*		*669*		
Shebanova and Lazor (2003)*:*	*193*	*306*				*538*		*668*		
Kumar et al. (2018):	*190.5*	*301*				*534*		*663.5*		
Thibeau et al. (1978):							*616*	*663*		
Mohammed et al. (2018):		*272*	*319*	*362*		*543*	*616*	*668*		
Legodi & de Waal (2007):		*297*				*523*		*666*		
Chamritski & Burns (2005):	*193*		*308*			*540*		*670*		
Jacintho et al. (2009):	*179*	*270*	*315*	*374*	*445*	*501*	*565*	*627*	*664*	*712*

Some of these data have been previously proposed by De Faria et al. To the data from Table 2 of Shebanova and Lazor (2003) we added those by Kumar et al., 2018 and Murugappan et al., 2014. The data by Jacintho et al. are given as reported in Soler and Qu, 2012. Also Mohammed et al., 2018, have provided data. The Raman spectroscopic analysis for magnetite is shown in their Table 1 and Figure 2; "the presence of the characteristic bands of magnetite Raman bands occurring at 272, 319, 543 and 668 cm^{-1} are consistent with references". The works mentioned by Mohammed and coworkers are those by Legodi and de Waal, 2007, Shebanova and Lazor, 2003, and Chamritski and Burns, 2005; we have considered the given references and found slightly different values of the positions of the peaks. Mohammed and coworkers add that "Bands of other material are noticed, [and] peaks observed at 702 cm^{-1} provide evidence due to the presence of hematite in agreement of mentioned in the literatures [Thibeau et al.], also bands at 458, 511, 591 and 764 cm^{-1} [exist], assigned to silicate"; and we can find also other compounds too (see references in Mohammed et al., 2018).

In the article by Shebanova and Lazor it is told that "some studies report two additional Raman bands at around 300 and 410–420 cm^{-1}". The researchers "note that these lines belong to the characteristic features of spectrum of hematite representing the $E_g(3)$ and $E_g(4)$ modes, respectively" (the reference mentioned is Beattie and Gilson, 1970). The reason is the *bivalent iron* which "makes magnetite easily prone to oxidation".

In De Faria et al., we find told that some of the reported magnetite peak positions (Hart et al., Verble, and Dünnwald and Otto) "are suspiciously close to the values expected for hematite. Thibeau et al. reported the Raman spectrum of a mixture of 90% Fe_3O_4 and 10% α-Fe_2O_3 by weight and the coincidence of this spectrum with that reported by Dünnwald and Otto is evident" (De Faria et al., 1997). The peak at 1322 cm^{-1}, "assigned to a hematite two-magnon scattering, is not a feature expected in a magnetite spectrum, reinforcing the assumption that hematite is present as a contaminant" (De Faria et al. 1997).

In the Figure 3(a) of De Faria et al., we can find the Raman spectrum "of a freshly fractured crystal face at room temperature", and "only the bands at 300, 532 and 661 cm^{-1} are observed". However, the laser power is affecting the sample; "when the laser power is raised to 7 mW new bands show up". Comparison to the spectrum of hematite, De Faria and coworkers conclude that hematite is formed and that "the spectral *changes are irreversible*". "Transformation of magnetite into hematite is a very common phenomenon in nature and is called *martitization*" (De Faria et al.). About the "conversions of magnetite to hematite and hematite to magnetite", see please Mücke and Cabral, 2005.

As noted by De Faria and coworkers, in Hart et al. (1976), it is possible to find a very weak feature at 472 cm^{-1}, feature assigned to magnon scattering and in agreement with neutron data. Let us consider again our Figure 2, where the deconvolution with q-gaussians is given. A band at 475 cm^{-1} is present.

Other data about magnetite nanoparticles and films

To approach the study of the iron oxide Raman spectra, ROD and RRUFF databases are perfect to properly visualize them. A Google search for images is, at the same time, intriguing and can help us to add further information. The plots provided by the search engine are very attractive. The first three images appearing in the search are from Hai et al., 2008, Yew et al., 2017, and Panta and Bergmann, 2015. Let us start considering the second reference.

In Yew et al., 2017, we can find proposed the Raman spectrum of magnetite nanoparticles (Fe_3O_4-NPs). In the Figure 7 by Yew et al. we can see shown the spectra of *K. alvarezii(seaweed)*/Fe_3O_4-NPs (coated NPs) and bare Fe_3O_4-NPs, and it is told that "both of the spectra show similar pattern". From the Figure, we can obtain the Raman shift of the peaks (coated and bare NPs), given at:

Coated	*212*	*272*	*388*	*474*	*585*	*1277*
Bare	*216*	*282*	*396*	*489*	*596*	*1294*

(in cm^{-1}). The authors say that the peak at 1294 cm^{-1} is the D-band: "This might be due to the presence of defects at the surface of NPs" (mentioning Mishra and Ramaprabhu, 2011). "The characteristic bands for Fe_3O_4 are located at approximately 670, 538 and 306 cm^{-1} (mentioning Murugappan et al., 2014). That is:

Murugappan et al.			*306*	*538*	*670*		*(we guess low laser power)*
Mishra and Ramaprabhu	*225.2*	*285.2*	*394.8*	*591.4*	*1336.4*	*1565.8*	*(we guess high laser power)*

Murugappan et al. data agree with the previously given data (Murugappan and coworkers do not provide information about laser equipment). But in the Figure 7 of Yew et al., we do not have these values. Yew and coworkers continue: "However, there are 3 peaks can be observed at around 388, 474 and 585 cm^{-1}

[values for coated NPs], which corresponded to the vibration modes of Fe-O bonds of Fe_3O_4-NPs" (mentioning Mishra and Ramaprabhu, 2011). Let us stress that the positions of the peaks, for coated and bare NPs given by Yew and coworkers, are far from the positions given by Murugappan et al., 2014, and by the literature that we have previously mentioned. However, Yew et al. conclude that "Raman spectrum can be found from literature [Murugappan et al., 2014] and thus the formation of Fe_3O_4-NPs *is confirmed*. The peaks at 212 and 274 cm^{-1} are due to the oxidation reaction occurred during Raman experiment" (Yew et al. mentioning Yuvakkumar and Hong, 2014). Yew and coworkers confirmed the presence of Fe_3O_4 NPs with positions of peaks which are different from those of the typical fingerprint of magnetite. Therefore, it is strictly necessary to consider in depth the articles mentioned by Yew et al.

Mishra and Ramaprabhu, 2011, do not give information about the Fe_3O_4 NPs that they use to decorate multiwalled carbon nanotubes. In their Figure 5, the researchers show the Raman spectra of functionalized MWNTs and Fe_3O_4-MWNT nanocomposite. We find the peaks of Fe_3O_4-MWNTs at:

225.2 285.2 394.8 591.4 1336.4 1565.8

(in cm^{-1}). "Raman spectroscopic analysis of the f-MWNTs shows a comparable intensity of the D-band …, [the D-band] is due to the presence of more defects at the surface of the MWNTs due to functionalization" (Mishra and Ramaprabhu, 2011). Defects are at the surface of nanotubes, not at the surface of Fe_3O_4 nanoparticles. Besides the D and G bands of nanotubes, we can find extra bands. "These extra peaks arise due to the formation of Fe_3O_4 nanoparticles over the surface of the MWNTs. Peaks at lower Raman shift (225.2, 285.2, 394.8 and 591.4 cm^{-1}) values may correspond to vibration modes of Fe–O bonds of Fe_3O_4 nanoparticles and Fe–C bonds at the surface of the MWNTs" (Mishra and Ramaprabhu are mentioning Tiwari et al., 2008, 2007). Then, let us consider these references.

In Tiwari et al., 2008, we can find Fe_3O_4 thin films. "Raman scattering was performed at room temperature to investigate the effect of substrate [no carbon substrates at all!] and thickness on the vibrational properties. The presence of various modes in Fe_3O_4 can be found in [Gasparov et al., 2000]" (Tiwari et al., 2008). Tiwari and coworkers observe three Raman modes: and these modes are about 310, 540 and 670 cm^{-1}. In their Figure 3 the Raman spectra of Fe_3O_4 films on different substrates are given and again we find peaks about 540 and 670 cm^{-1}. In Tiwari et al., carbon is not present or mentioned (see more details in the Appendix about Tiwari et al. works).

Yew et al. are telling that "Raman spectrum can be found from literature", mentioning Murugappan et al., 2014. Murugappan and coworkers are providing data about synthesized Fe_3O_4 NPs with oleic acid as surfactant. "Raman spectroscopy was performed to "fingerprint" the vibrational and rotational bands that are specific to Fe_3O_4. Several Raman spectroscopic studies [see footnote[1]] of Fe_3O_4 have been performed, and the characteristic bands for Fe_3O_4 are located at approximately 670, 538, and 306 cm^{-1}". In the Figure 2 of the article by Murugappan and coworkers the Raman spectrum of the synthesized Fe_3O_4 nanoparticles has been proposed with the spectra of magnetite and hematite. "It can be seen that the spectrum of the *synthesized Fe_3O_4 nanoparticles closely resembles that of the pure magnetite* sample. The absence of bands at 205 and 268 cm^{-1} further indicated that the synthesized material was indeed Fe_3O_4 and not Fe_2O_3". The "Fe_3O_4 nanoparticles are susceptible to oxidation, which would result in a loss of magnetization. The spectrum suggested that the synthesized nanoparticles were not oxidized" (Murugappan et al., 2014). In Sparavigna, 2023, when discussing the Fe_3O_4 iron oxide for improving EMI-SE, I have encountered a lot of encapsulated Fe_3O_4 NPs; encapsulation can prevent oxidation, such as their coating (Bruschi & de Toledo, 2019, Aisida et al., 2020).

[1]) Murugappan and coworkers are mentioning Shebanova and Lazor, 2003, Verble, 1974, De Faria et al., 1997, Gasparov et al., 2000, Graves et al., 1988.

Here the data from Murugappan and coworkers (in cm^{-1}):

Hematite:	*205*	*268*	*328*	*560*	
Magnetite:		*311*	*360*	*488*	*677*
Magnetite NPs:		*314*	*364*	*500*	*679*

Let us also consider the article by Yuvakkumar and Hong. In the Figure 1b of their article we can see the Raman spectrum of green synthesized Fe_3O_4 nanoparticles (to synthesize the particles the rambutan peel waste extract has been used as a green ligation and chelating agent). In fact, no specific data about the Raman shift are given in their figure. It is told that "The characteristic bands at 670 and 318 cm^{-1} were attributed to the Fe-O normal vibrations of magnetite Fe_3O_4. … The peaks at 300 and 410–420 cm^{-1} were relevant to an oxidation reaction during a Raman experiment. The bands at 538 (T_{2g}), 306 (E_g) and 194 cm^{-1} (T_{2g}) were characteristics of magnetite Fe_3O_4 [Venkateswarlu et al., 2014]. The result proves that the synthesized iron oxide is Fe_3O_4" (Yuvakkumar and Hong).

What is the iron oxide in Yew et al.? It does not possess the fingerprint of magnetite. The same for the iron oxide by Mishra and Ramaprabhu. Is it enough to observe two peaks of oxidation to conclude the presence of magnetite?

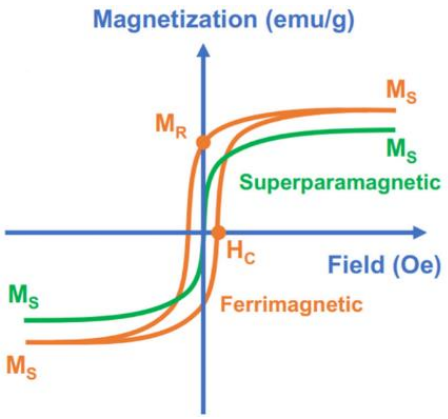

Fig.6: The image shows the magnetization versus the applied field (M–H) for superparamagnetic (green color) and ferrimagnetic (orange) Fe_3O_4 nanoparticles. Image courtesy Nguyen et al., 2021, article distributed under https://creativecommons.org/licenses/by/4.0/ .

Superparamagnetism

Before discussing the role of the laser power in the measurements by Yew and coworkers, let us introduce the magnetism in Fe_3O_4 NPs. In Blaney, 2007, we can find the detailed description of magnetite (Fe_3O_4). A section of the article explores the bulk properties of it. Referring to Cornell and Schwertmann, 1996, Lee Blaney is evidencing a semi-conductor behavior, bordering the conductor (metallic) behavior, of the magnetite. A semimetallic behavior of magnetite is also supported by the relatively low bandgap (0.1 eV) of the material (Cornell & Schwertmann, 1996). The Curie temperature is at 850 K. Below the Curie temperature, we can find the magnetite as a ferrimagnetic material (Cornell & Schwertmann, 1996; see our Appendix C for the other iron oxides). "When the Curie temperature is attained, a superparamagnetic behavior is observed". 850 K is the Curie temperature of the bulk

material, and we are quite above the room temperature; however, if we consider the particles, as the particle size decreases, the behavior tends towards a paramagnetic or superparamagnetic magnetization. The decreasing of the particle size reduces ferrimagnetic behavior and enhances superparamagnetic behavior (Blaney, 2007).

The bulk magnetite is ferrimagnetic, "generated by parallel alignment of magnetic moments on tetrahedral sites and anti-parallel alignment of ferrous and ferric spins on octahedral sites" (Blaney, 2007). In the Figure 10 by Blaney, we can see a generic ferrimagnetic hysteresis loop, with coercivity and remanence (retentivity). "As particle size is decreased, the amount of exchange-coupled spins resisting spontaneous magnetic reorientation is decreased, tending towards paramagnetic or superparamagnetic magnetization" (Blaney, 2007, mentioning Kiely, 2006). As previously told, when the magnetite particle size decreases, the ferrimagnetic behavior is reduced and the superparamagnetic behavior enhanced. Increasing the temperature, the thermal energy facilitates "magnetic reorientation, or superparamagnetic magnetization" (Blaney mentioning Kiely). "In accordance with superparamagnetic behavior, magnetite nanoparticles exhibit zero coercivity and remanence in hysteresis loops as illustrated in Figure 11 [of Blaney, 2007]. Coercivity slowly builds as magnetite particle diameter increases". In the caption of the mentioned figure, it is told that the absence of hysteresis loop is implying superparamagnetism (Hou et al., 2003).

"The superparamagnetic (SPM) and ferrimagnetic (FM) behaviors of Fe_3O_4 NPs depend on size, shape, crystallinity, and surface properties and are even affected by synthetic methods" (Nguyen et al., 2021, and references therein).

In the Figure 8 by Yew et al., we can find the magnetization curves of K. alvarezii/Fe_3O_4-NPs and bare Fe_3O_4-NPs at room temperature. In both curves, the hysteresis is absent and therefore the nanoparticles produced by Yew and coworkers are displaying a superparamagnetic behavior.

Laser power (debris fingerprint)

In Slavov et al., 2010, we can find the Raman spectroscopy used to investigate the magnetite nanoparticles dispersed in two types of β-cyclodextrin suspensions. "The effect of elevating laser power on the structural stability and chemical composition of magnetite in the ferrofluids is discussed. … Powder samples undergo total phase transition from magnetite to hematite at laser power of 1.95 mW. … The Raman spectra revealed that the main phase of the magnetic [particle] core … is magnetite. That is indicated by a strong and non-diminishing in intensity peak at 670 cm^{-1}" (Slavov et al., 2010). "A second phase is present at the nanoparticle's surface with Raman spectroscopy unveiling *maghemite-like and small fractions of goethite-like structures*" (Slavov et al., 2010).

Slavov and coworkers tested the magnetite by increasing the laser power from 0.9 to 9.0 mW. "The characteristic peak positions of magnetite (Fe_3O_4) and its possible oxidation byproducts, maghemite (γ-Fe_2O_3) and hematite (α-Fe_2O_3) *determined the Raman region of interest*" in Slavov et al. investigation. The range is 100–1200 cm^{-1}. "For correct assignment of the band positions … and for phase identification," Vlasov and coworkers used the following peaks (in cm^{-1}): Magnetite 193 (weak), 306 (weak), 538 (weak), 668 (strong); Maghemite 350 (strong), 500 (strong), 700 (strong); Hematite 225 (strong), 247 (weak), 299 (strong), 412 (strong), 497 (weak), 613 (medium).
"The analysis of all spectra reveals the destructive influence of the atmospheric oxygen on the structural stability of even coated magnetite nanoparticles. *For the uncoated magnetite particles, a timeline of less than 30 days meant a total transition towards maghemite. … The oxidation process starts at a very early stage after formation of the nanoparticles*" (Slavov et al., 2010).

In the Figure 3 of the article by Slavov and coworkers, we can see the Raman spectra of powdered magnetite nanoparticles obtained with a laser power of 0.060 mW and a laser power of 1.95 mW.

The peaks are (in cm^{-1}):

0.060 mW: *383* *463* *519* *670*

1.95 mW: *215* *276* *386* *584* *1280*

Here we are ready to consider again the data from Yew et al., 2017, about bare and coated nanoparticles.

Coated NPs: *212* *272* *388* *474* *585* *1277*

Bare NPs: *216* *282* *396* *489* *596* *1294*

We can tell that we are observing the debris fingerprint of Fe_3O_4 nanoparticles, because the laser power was enough high to cancel the typical peaks of magnetite. The Fe_3O_4 particles prepared by Yew and coworkers are superparamagnetic. However, let us stress that hematite can have a superparamagnetic behavior too. "For hematite in the nanoparticle morphology, [the bulk] characteristics are affected by the particle size and shape. Spherical particles with diameter smaller than 25–30 nm are superparamagnetic and the Morin temperature is lowered significantly or even suppressed" (see Lee et al., 2014, and references therein). Yew et al. definitely concluded about magnetite thanks to the XRD (X-ray diffraction) analysis (see please the Figure 3 in their article, comparing with the following figure).

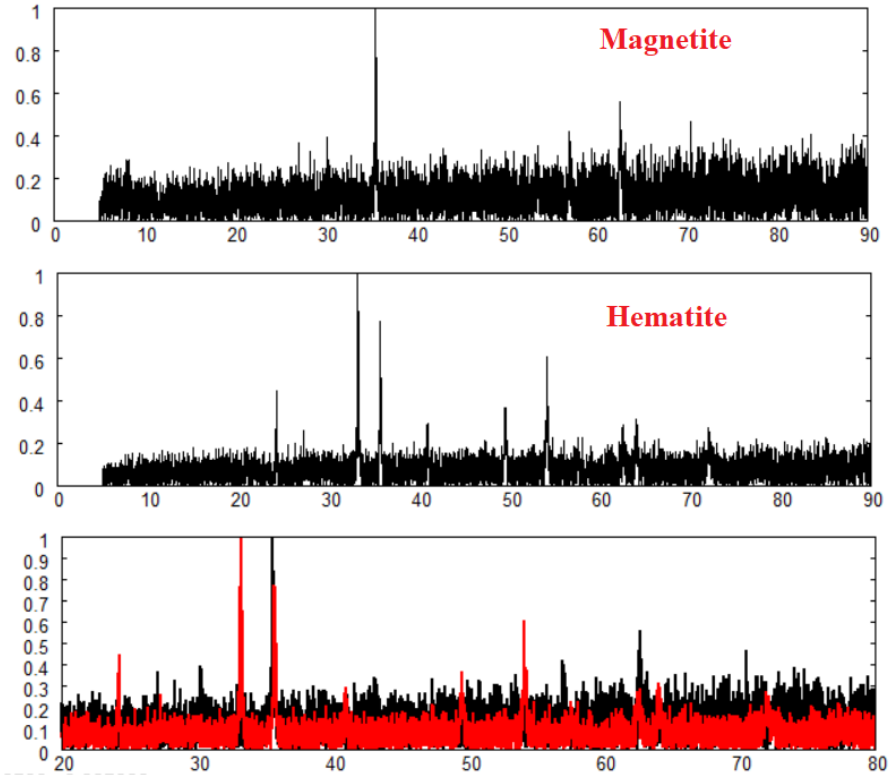

Fig. 7: XRD data for Magnetite and Hematite (in the lower panel, in black data of magnetite and in red of hematite). Data from RRUFF, https://rruff.info/magnetite/display=default/R060191 and https://rruff.info/hematite/display=default/R040024 .

About the laser power, let us add what we can find in Panta and Bergmann, 2015: "it is known that magnetite has a weak Raman scattering, especially for lower laser powers". Increasing the laser power induces phase transformations. Besides the influence of power, Panta and Bergmann note that also the wavelength is relevant (peaks, in cm^{-1}):

Laser 512 nm:	*215*	*276*	*398*	*487*	*654*	*1300*
Laser 785 nm:					*670*	

Annealing

Yew and coworkers created NPs in the following manner. An iron salt solution was prepared and added into the seaweed extract solution. The pH of the solution was regulated by adding NaOH solution under continuous stirring. "After the reaction has completed, the as-synthesized Fe_3O_4-NPs were isolated by a permanent magnet and washed for a few times with deionized water. The washed Fe_3O_4-NPs were dried in an oven at approximately 70 °C for 24 h. Consequently, the dried sample were stored for further characterization" (Yew et al., 2017). Is the drying in oven producing a phase transition to hematite? In the case of Yew and coworkers' particles, the answer is negative (XRD tells us: magnetite).

In Dar and Shivashankar, 2014, we can find how annealing processes can affecting the iron oxide phases. Dar and Shivashankar, 2014, produced magnetite, maghemite, and hematite nanoparticles from amorphous iron oxide nanoparticles with two different sizes (<5 nm and 60 nm). "The transformation of the as-prepared amorphous powders into Fe_3O_4 and Fe_2O_3 phases (γ and α) is achieved by carrying out controlled annealing at elevated temperatures under different optimized conditions." (Dar and Shivashankar). "Unlike Fe_3O_4, Fe_2O_3 exists in four different crystalline polymorphs, namely, γ-Fe_2O_3, β-Fe_2O_3, ε-Fe_2O_3 and α-Fe_2O_3," among which maghemite and hematite have been largely investigated. *The maghemite is a ferrimagnetic material* at room temperature. "By contrast", hematite "is weakly ferromagnetic at room temperature due to the Dzyaloshinsky–Moriya mechanism and is antiferromagnetic below 263 K (referred to as the Morin temperature, T_M)" (Dar and Shivashankar, 2014). Dar and Shivashankar studied the magnetism of the nanoparticles they prepared.

Fe_3O_4 is obtained after annealing the amorphous iron oxide, at 300 °C for 12 h under N_2 atmosphere. The γ-Fe_2O_3 phase is obtained after annealing Fe_3O_4 at 200 °C for 4 h under ambient conditions. The α-Fe_2O_3 phase is obtained after annealing the maghemite at 600 °C for 6 h under ambient condition. In the Figure 5 by Dar and Shivashankar, we can see the Raman spectrum of magnetite nanoparticles, with peaks at about 330, 537 and 663 cm^{-1}. The maghemite NPs have peaks around 340, 492 and 703 cm^{-1}. And the hematite nanoparticles have peaks at 225, 245, 290, 407, 491, 608 and 654 cm^{-1}.

Exposed to air

In Hai et al., 2008, the problem of the stability of iron-based magnetic fluids have been addressed. The researchers studied the oxidation process, a process that "depends on the materials that make the nanoparticles, [and] the diffusion of oxygen atoms from the environment to the magnetic nanoparticles, which mainly depends on the viscosity of the solution and the surfactant that coats the nanoparticles". Hai and coworkers "suggest three ways to protect nanoparticles from oxidation: (a) using highly viscous carrier liquid (b) using relevant surfactants and (c) substitution of Ni^{2+} and Co^{2+} for Fe^{2+} in magnetite" (Hai et al., 2008).

In the Figure 3 of Hai et al. article, the Raman spectra of Fe_3O_4 nanoparticles before and after exposure in air for 20 days are given.

Here the peaks (in cm^{-1}):

Before				*665*		
After	*185*	*358*	*488*	*665*	*1170*	*1380*

Magnetite and maghemite together

In Chourpa et al., 2005, we can find a study of chemical and structural properties of ferrite-based nanoparticles. "The nanoparticles were synthesised as aqueous magnetic fluids by co-precipitation of ferrous and ferric salts. Dehydrated particles corresponding to co-precipitation (CP) and oxidation (OX) steps of the magnetic fluid preparation have been compared in order to establish oxidation-related Raman features" (Chourpa et al., 2005). Because of the "risk of laser-induced conversion of magnetite into hematite", the study is made with different "laser power and exposure to oxygen. Under hematite-free conditions, the Raman data indicated that nanoparticles consisted of magnetite and maghemite, and no oxyhydroxide species were detected" (Chourpa et al.). To obtain the relative spectral contribution of maghemite and magnetite, a deconvolution with Lorentzian profiles was made.

The Raman spectra had been made by a laser excitation at 632.8 nm. "Laser power delivered by the laser (15 mW) was reduced via filters (optical densities 0.3, 0.6, 1, 2, 3 and 4)." A laser power at the sample of 0.4 mW was avoiding the sample degradation (Chourpa et al.). The required chemistry for the investigation by Chourpa and coworkers is ferric and ferrous chloride and nitrate, potassium dichromate, nitric acid, and others provided by Fluka. "Black iron oxide (iron(II,III)) was supplied by Prolabo (France)". "Before studying the nanoparticles, [Chourpa and coworkers] analysed bulk samples of commercially purchased black iron oxide (Fe_3O_4 + Fe_2O_3)". The researchers observed that, according to the investigated localization, the Raman spectra "exhibited variable mixtures of two or three oxides": magnetite, maghemite and hematite. In the Figure 1 by Chourpa et al., we can find the confocal micro-Raman measurements with black iron oxide. The peaks are at:

Bulk magnetite:		*194*			*303*		*528*	*662*
Magnetite contaminated:	*225*	*247*	*292*	*411*	*496*	*662*		*1318*

(in cm^{-1}). *The magnetite is contaminated with laser-independent hematite* (experimental conditions with 0.4 mW of 632.817 nm laser line). The spectra of bulk and contaminated magnetite show the magnetite band at 662 cm^{-1}. "The low-power laser irradiation did not produce any significant variation of hematite/magnetite ratio with time. In contrast, the signal of hematite induced with double the laser power … was progressively growing over that of magnetite. … With 1.6 mW and above, the increase of the hematite signal was almost instantaneous and was accompanied by a disappearance of the magnetite band at 662 cm^{-1}. *The resulting hematite bands were broader and shifted to lower frequencies*" (Chourpa et al., 2005). In the Figure 2 by Chourpa and coworkers, we can find the peaks of the Raman spectra of hematite generated by laser power of 0.8 mW and 1.6 mW.

0.8 mW	*219*	*283*	*397*	*597*	*671*
1.6 mW	*213*	*271*	*376*	*578*	

Chourpa and coworkers "aimed to prepare *superparamagnetic nanoparticles free of antiferromagnetic hematite*." They "did not detect any laser-independent hematite in the samples of synthetically prepared nanoparticles. *Compared to the bulk oxide, the nanoparticles appeared generally somewhat more resistant to hematite formation* upon laser heating: they resisted laser powers of more than 0.4 mW

during 1 hour without any spectral change". The researchers also note that, besides the laser power, an exposure to oxygen "is essential for the formation of hematite." Chourpa and coworkers suggest also that the observed "laser-stimulated hematite was formed from pre-initialised oxidation sites (domains rich in oxygen and hematite germs)".

The lacunar phase maghemite is also considered in detail. "The great diversity of spectra reported in the literature illustrates the difficulty in obtaining a representative Raman spectrum of pure maghemite". The most part of literature shows the maghemite with three broad peaks at around 360–380, 500 and 660–720 cm^{-1}. "In practice, these bands are most often accompanied by bands testifying to the presence of other iron oxide or oxyhydroxide species" (Chourpa et al., 2005). To determine the peaks of maghemite, Chourpa and coworkers opted for nanoparticles. In the Figure 4 and in the Table 1, the Raman spectral data for the CP and OX nanoparticles are available, with assignments.

	magnetite	*maghemite*	*magnetite*	*maghemite*
CP	*195*	*330 383*	*496 671*	*712 1360*
OX	*195*	*330 383*	*499 671*	*712 1400*

We can see magnetite/maghemite Raman peaks in Oraby et al., 2022. The article is proposing a study of rGO/Fe_3O_4 hybrid nanocomposites, encapsulated in polyurethane (rGO, reduced graphene oxide). The study aims to improve EMI shielding effectiveness. "The acquired fillers were encapsulated in the polyurethane foam matrix with different loading percentages (wt%) to evaluate their role in EMI shielding. … The obtained results revealed that the Fe_3O_4@rGO composites displayed superparamagnetic behavior and acceptable electrical conductivity value" (Oraby et al., 2022). Oraby and coworkers are giving the Raman spectrum in their Figure 3a, "for the prepared magnetite cluster nanoparticles. The peaks marked with the dashed black lines refer to the vibrational modes of Fe_3O_4 magnetite and the red ones represent maghemite (γ-Fe_2O_3). It is clear that the main five peaks for magnetite appeared at 196, 306, 460, 538, and 668 cm^{-1}, … . On the other hand, the main three peaks of maghemite appeared at 350, 500, and 700 cm^{-1}, … In this context, other characteristic features of the materials such as the black coloration of its powders or their strong response to external magnetic fields should be considered" (Oraby et al, 2022).

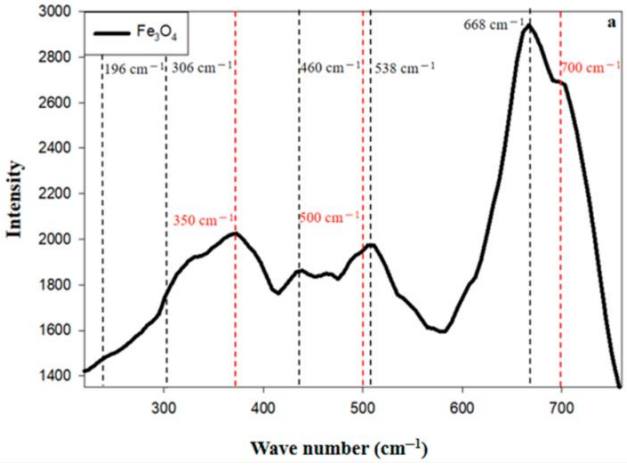

Fig. 8: The Raman spectrum as given by Oraby and coworkers. The article, available at the following link https://www.mdpi.com/2079-4991/12/16/2805, is provided under the Creative Commons Attribution (CC BY) license (https://creativecommons.org/licenses/by/4.0/).

Nanosizing

In Owens and Orosz, 2006, we can find a study about the "effect of nanosizing on the Raman spectra … of the hematite phase of Fe_2O_3 produced by laser decomposition of Fe_3O_4 nanoparticles". In the Figure 2 of their article, we can see analyzed the Raman spectra for bulk and nanoparticles of Fe_3O_4 recorded at room temperature. "No frequency shifts or broadening of the Raman lines are observed in the nanoparticles compared to the bulk material". In particular, the Raman spectra were obtained with a 632 nm 20 mW laser, with density filter D=4. Owens and Orosz concluded that a "9 nm nanosizing is not affecting the vibrational frequencies in the Fe_3O_4 nanoparticle" (see also references therein).

The peaks in their Figure 2 are (in cm^{-1}): *432 495 604 711*

Increasing the laser power, the "bulk Fe_3O_4 converts to the hematite phase of Fe_2O_3" (Owens and Orosz, mentioning Shebanova and Lazor). In the Figure 3 by Owens and Orosz we can find the spectra obtained from bulk Fe_3O_4 and nanoparticles of Fe_3O_4, with the same focused laser without the filter. Changing the laser intensity, "new Raman lines have appeared. The frequencies of the new spectra are in good agreement with the frequencies of the previously reported Raman spectra of the Fe_2O_3 hematite phase" (Owens and Orosz are mentioning Hart et al. and Beattie and Gilson).

Bulk	*223*	*288*	*407*	*431*	*493*	*606*	*657*	*711*
Nanoparticles	*218*	*280*	*394*	*432*	*495*	*602*		*711*

Maghemite

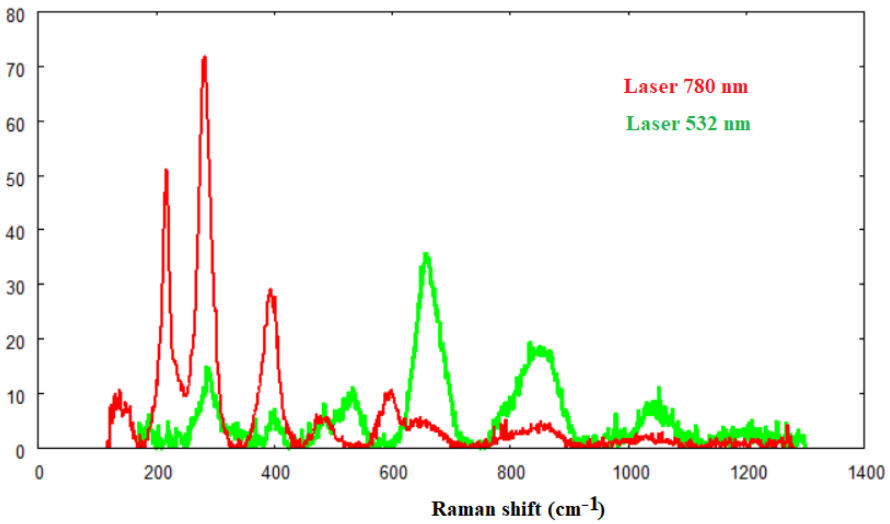

Maghemite spectra are proposed by RRUFF for sample R140712, source Rock Currier, owner RRUFF. The sample is a black aggregate of small to fine grains. "The identification of this mineral has been confirmed only by single crystal X-ray diffraction". Chemistry: $(Fe^{3+}_{0.67}\square_{0.33})Fe^{3+}_2O_4$, where the represents a vacancy. https://rruff.info/maghemite

Fig.9a: Maghemite Raman spectra from RRUFF Project website.

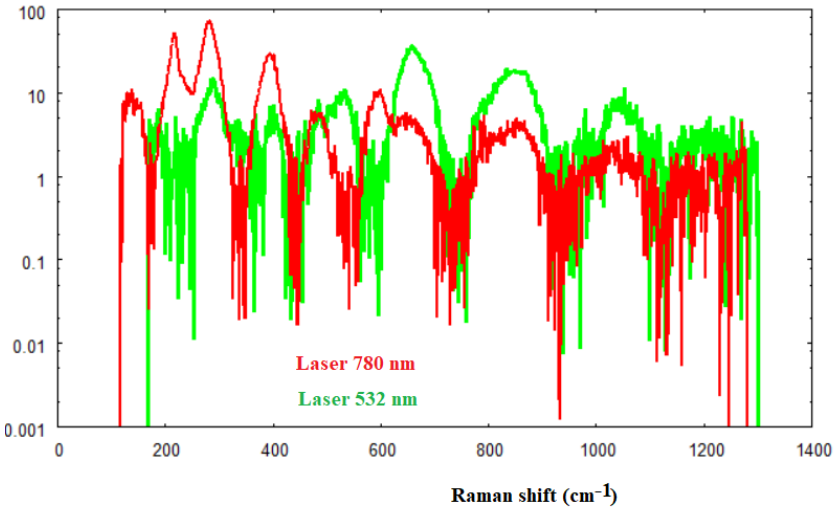

Fig.9b: The same as in Fig. 9a in semi logarithmic scale.

Monika Hanesch, using a confocal-Raman spectrometer equipped with a Nd-YAG laser (532.2 nm), studied the maghemite. "The laser power was kept low because 1 mW laser power led to the transformation of the maghemite to haematite and, hence, the measurement of haematite spectra". In her Figure 7, M. Hanesch is giving maghemite bands identified at 350, 512, 664, 726 and 1330 cm^{-1}. "The bands coincide with those measured by Jacintho et al. (2007)". And small peaks of hematite can be observed sometimes (224, 294 and 411 cm^{-1}). Let us remember also the data from Chamritski and Burns (2005): 350, 500 and 700 cm^{-1}.

Frequencies Of Iron Oxide Raman Bands

Compound		Band Positions (cm^{-1})				
α-FeOOH	goethite	298	397	414	474	550
γ-FeOOH	lepidocrocite	252	380			
FeO	wüstite	616	663			
Fe_3O_4	magnetite	616	663			
α-Fe_2O_3	hematite	227	245	293	298	414
		501	612			

The Table I from Thibeau, R. J., Brown, C. W., & Heidersbach, https://apps.dtic.mil/sti/pdfs/ADA056298.pdf

Goethite and Lepidocrocite (α-FeOOH and γ-FeOOH)

In Thibeau et al., 1978, the Raman spectra of FeO, Fe_3O_4, α-Fe_2O_3, α-FeOOH, and γ-FeOOH, which are "the common products of iron oxidation", are given. "Raman spectra of the oxides of iron can be obtained with little difficulty using conventional instrumentation. … Spectra of thin surface films are

identical to those of the pure compounds comprising the films" (Thibeau et al., 1978). Thibeau and coworkers add that it is observed "considerable variation in intensity of Raman scattering from these oxides. The black compounds, FeO and Fe_3O_4, give weak spectra, whereas those which are lighter in color, α-Fe_2O_3, α-FeOOH, and γ-FeOOH, give stronger spectra".

The crystalline α-FeOOH goethite was obtained precipitating by hydrolysis a ferric oxalate solution, with additional adjusting $NaHCO_3$ solution. The hydrolysis of a ferrous chloride solution is giving γ-FeOOH lepidocrocite. In the Table I by Thibeau et al., we find the spectra (in cm^{-1}).

Goethite:	*298*	*397*	*414*	*474*	*550*
Lepidocrocite:	*252*	*380*			

The spectra of Goethite and Lepidocrocite are proposed also by Monika Hanesch, 2009.

Goethite :	*244*	*299*	*385*	*480*	*548*	*681*
Lepidocrocite:	*250*	*348*	*379*	*528*	*650*	

According to Hanesch, the measured spectrum of synthetic goethite "corresponds to the spectra of this mineral shown in the literature" (M. Hanesch is mentioning Oh et al., 1998). "The combination of a strong peak at 385 cm^{-1} with clear peaks at 244, 299, 480, 548 and 681 cm^{-1} is easy to distinguish from any other spectrum. Synthetic goethite was measured with a laser power of 0.1 mW" (Hanesch, 2009). For the synthetic lepidocrocite too, Hanesh finds the same bands known from literature (Oh et al. 1998). The sample is "stable also at 0.1 mW laser power". According to Hanesch, the lepidocrocite "is especially interesting … because maghemite is produced by heating the lepidocrocite to 400 °C".

The shape of the nanoparticles

There is a manner to distinguish goethite nanoparticles, and it is the observation of their shape. Goethite has needle-like or acicular shape particles (pure goethite, needle-like) (Legodi & de Waal, 2007). Magnetite and hematite particles have a pseudocubic shape, according to Legodi and de Wall. However, spherical and rod-like magnetite nanoparticles have also been synthesized (Baghshahi & Yousefi, 2021). In the Fig.8, we are showing the rod-like magnetite nanoparticle, prepared by Cheng et al., according to the method by Fortin et al., 2007. Recently, Fe_3O_4 particles acicular and octahedral structures have been disclosed too (Shu et al., 2021). Even nanotubes - Fe_3O_4@C core–shell nanotubes - have been prepared (Li et al., 2014). For more information about the shapes of particles, see Cornell and Schwertmann, 2003.

As explained by Martina et al., 2022, the goethite nanoparticles are needle-like structures, "naturally asymmetric and anisotropic and with antiferromagnetic properties". We could tell that these particles are analogous to the rod-like molecules of liquid crystals. "Lemaire et al. widely investigated aqueous suspensions of goethite nanorods giving rise to stable *isotropic and nematic phases* showing peculiar magnetic properties because goethite nanorods align parallel to a weak magnetic field but perpendicular to a strong field" (Martina et al., and references therein).

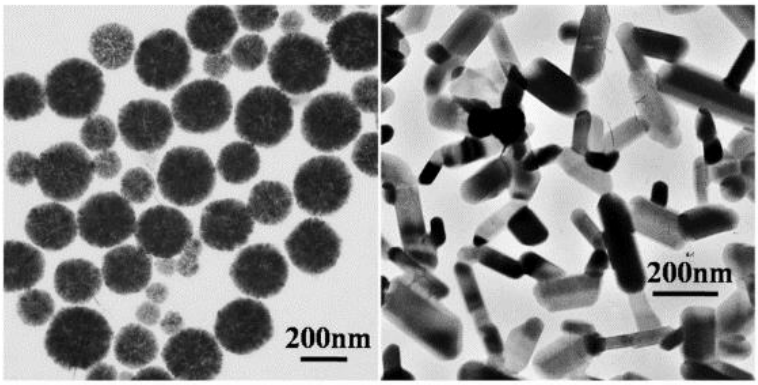

Fig. 10: Spherical and rod-like magnetite nanoparticle. Image courtesy from the article by Cheng, D., Li, X., Zhang, G., & Shi, H. © 2014 licensee Springer. It is an Open Access article distributed under the terms of the Creative Commons Attribution License 4.0, which permits unrestricted use, distribution, and reproduction in any medium, provided the original work is properly credited.

Lepidocrocite in ROD database

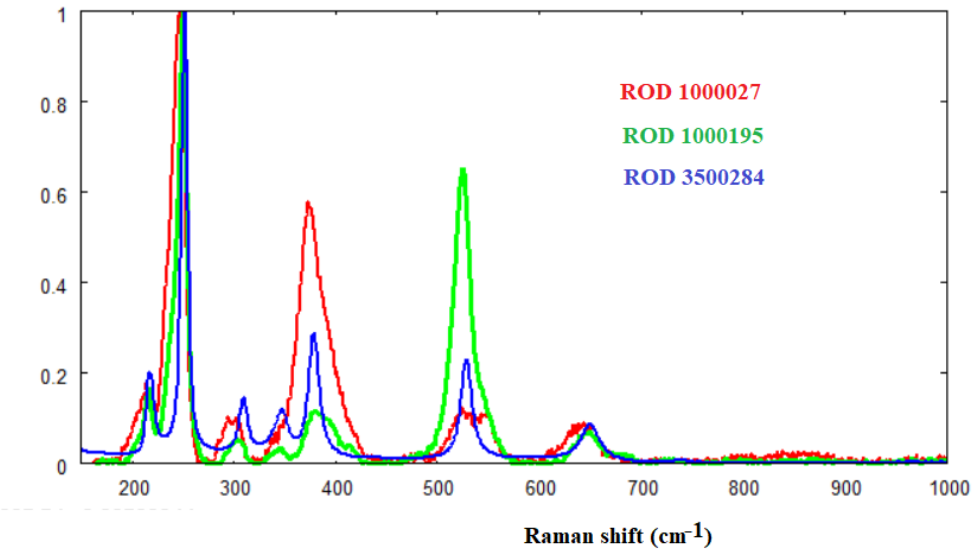

Fig. 11a: Raman spectra of Lepidocrocite from Raman Open Database (ROD). ROD 1000027 (laser 780 nm) data courtesy Wyckoff, 1963, https://solsa.crystallography.net/rod/1000027.rod ; ROD 1000195 (laser 532) data courtesy Wyckoff, 1963, https://solsa.crystallography.net/rod/1000195.rod ; and ROD 3500284 (laser 633 nm) data courtesy Kumar et al., 2019, https://solsa.crystallography.net/rod/3500284.rod

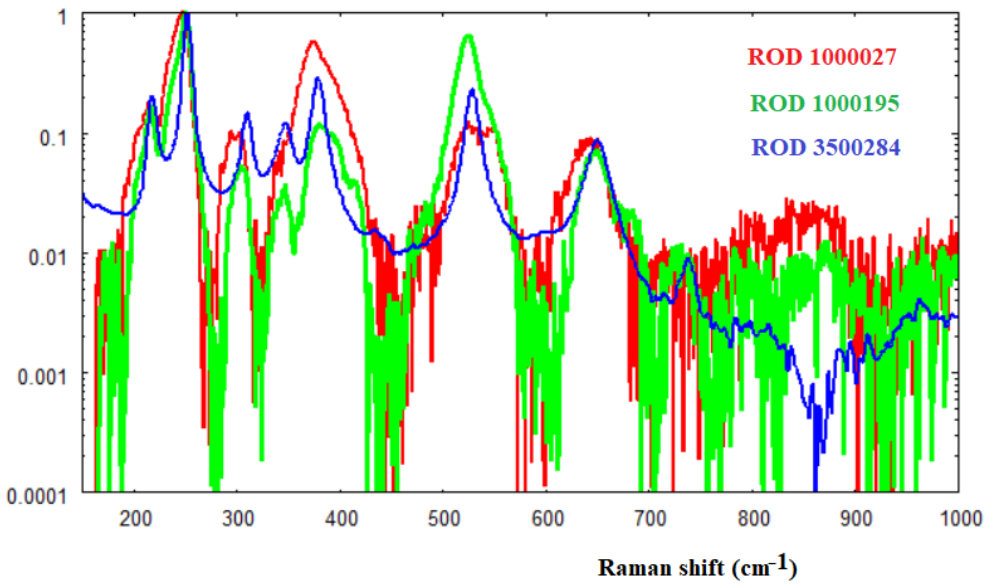

Fig. 11b: The same as in Fig.11a with semi log scale.

Here the peaks (in cm^{-1}):

ROD 1000027:	*215 247 (strong)*	*294 302*	*373 (strong)*	*518 525 531 538 545*	*644 659*
ROD 1000195:	*217 250 (strong)*	*306 347 380*		*527 (strong)*	*650*
ROD 3500284:	*217 252 (strong)*	*310 347 378 (strong)*		*528 (strong)*	*650*

Fitting the bands

Lepidocrocite is the occasion for a discussion about the fitting of the Raman spectra.

Let us consider the spectrum by Kumar et al., 2019, https://solsa.crystallography.net/rod/3500284.rod, and fit the processed data by means of q-Gaussians. This is the same what we can do as for data available in literature, usually given just in the processed form, without any information about the applied processing method of the raw data. The result of the q-Gaussian fitting is shown in the Fig.11c, for a part of the spectrum. The misfit is evidencing that a further investigation could be interesting for the largest peak, that is the second peak from the left. But before, we compare the q-Gaussian fitting with fits obtained with Lorentzian and Gaussian functions.

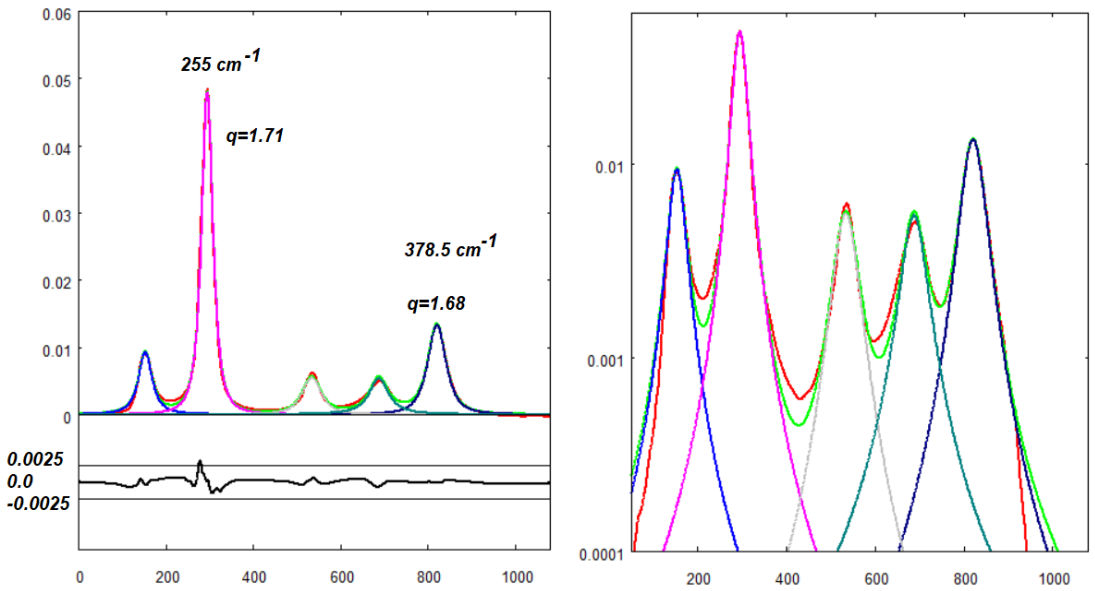

Fig. 11c: Best fit (green) with q-Gaussians (components in different colors) of a part of the spectrum of lepidocrocite ROD 3500284 (laser 633 nm) data (red) courtesy Kumar et al., 2019, https://solsa.crystallography.net/rod/3500284.rod . On the right the same in semi log scale.

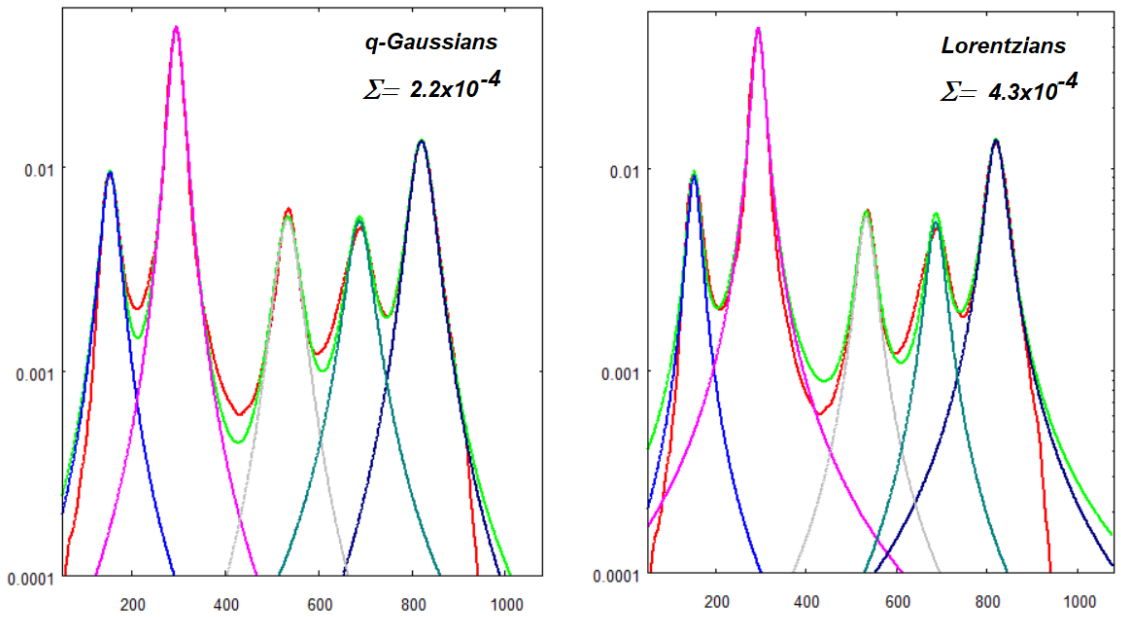

Fig. 11d: Best fit (green) with q-Gaussians on the left, and with Lorentzian functions on the right, in semi log scale. The fitting calculation is obtained by minimizing the sum of the squares of the deviations ($2.2x10^{-4}$ on the left, $4.3x10^{-4}$ on the right, the sum is made on the equally spaced points of the x-axis used for fitting and shown in the figure). Note that the wings of the bands are different.

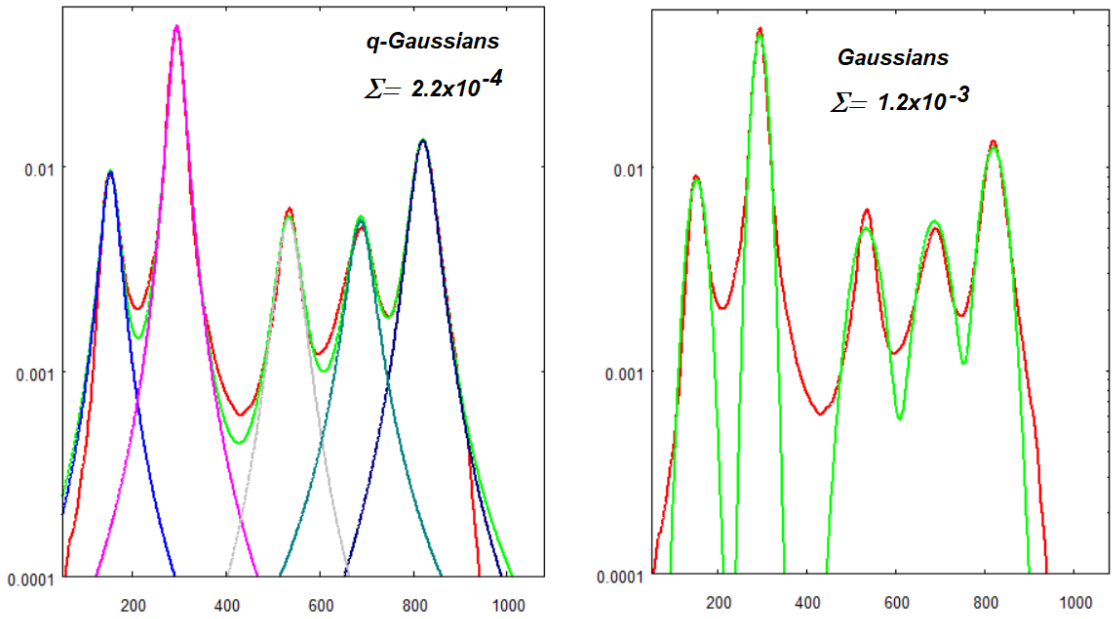

Fig. 11e: Best fit (green) with q-Gaussians on the left, and with Gaussian functions on the right. The fitting calculation is obtained by minimizing the sum of the squares of the deviations ($2.2x10^{-4}$ on the left, $1.2x10^{-3}$ on the right). Components are not shown.

In the Figures 11d and 11e we have compared the best fits made with q-Gaussians, Lorentzian functions and Gaussians. The sum of the squares of the deviations has its lowest value for the q-Gaussians. In the case of the Lepidocrocite spectrum, the resulting q-Gaussian line shapes are closer to Lorentzian than to Gaussian functions.

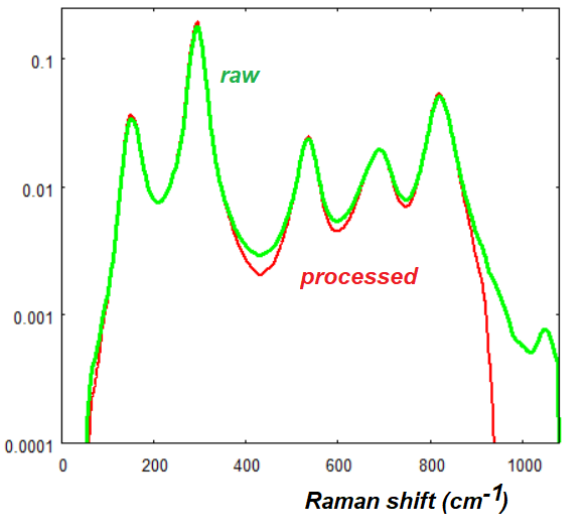

Fig. 11f: Processed (red) and raw (green) data.

For the previous comparisons, we have used the processed data. As shown by the image in the Fig. 11f, there are some differences between processed and raw data. In the case we consider the raw data, the results are given in the following plots. The results (Fig.11g) are consistent with those previously given.

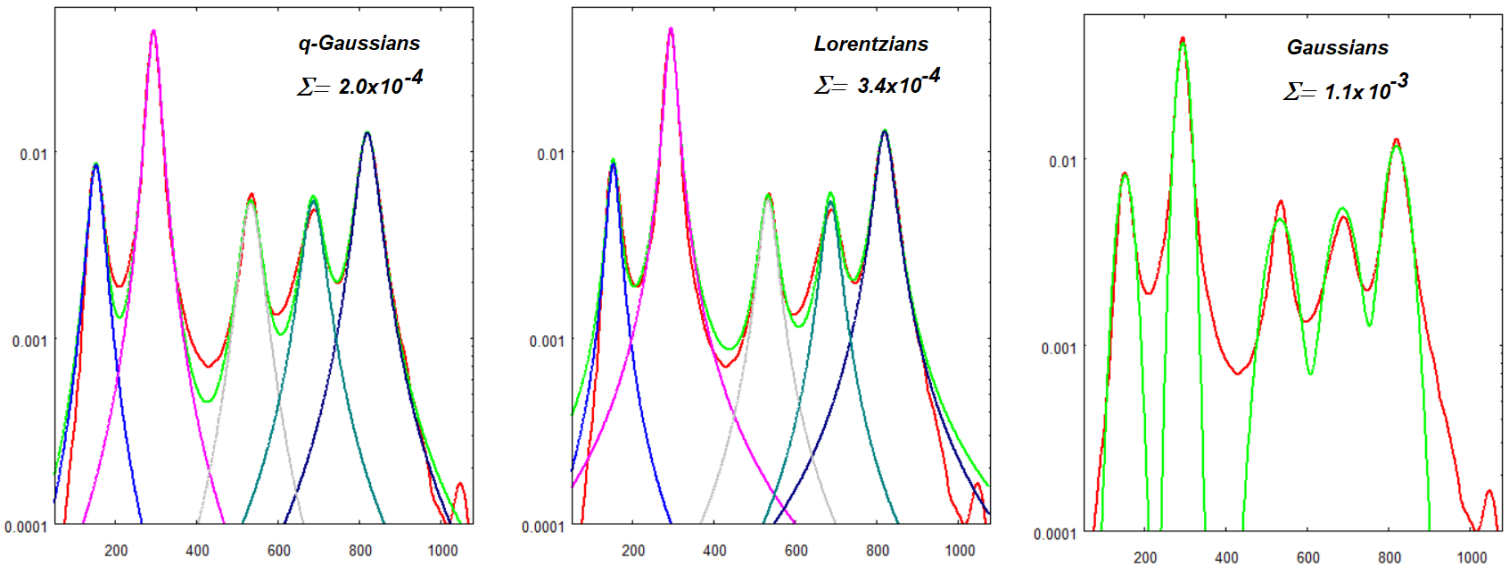

Fig. 11g: Best fit (green) of the raw data (red) with q-Gaussians on the left, Lorentzian functions in the middle, and Gaussians on the right.

We have seen that the q-Gaussians are providing a better fitting result, in comparison to Lorentzian and Gaussian functions, for processed and raw data. Considering the first two peaks of the spectrum, let us compare the q-Gaussian fit with that we can obtain with pseudo-Voigt functions. Pseudo-Voigt functions are linear combination of Lorentzian and Gaussian functions (Meier, 2005).

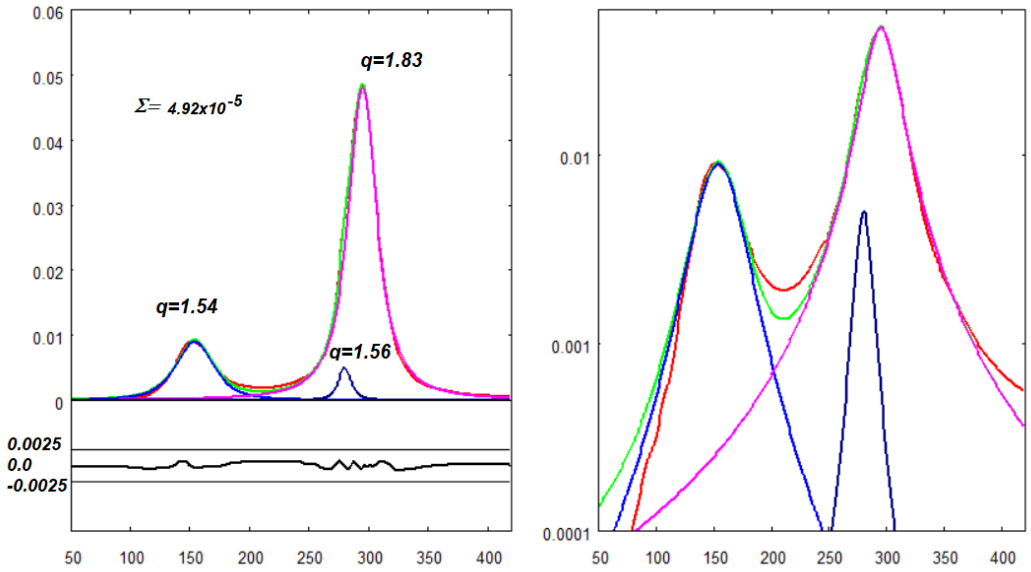

Fig. 11h: Best fit with three q-Gaussians of the first two peaks shown in Fig. 11c. The sum of the squares of the deviations is equal to $4.92x10^{-5}$. The sum is made on the interval shown in the figure. Note that a component has been added in the fitting procedure, to consider the slight asymmetry of the larger peak.

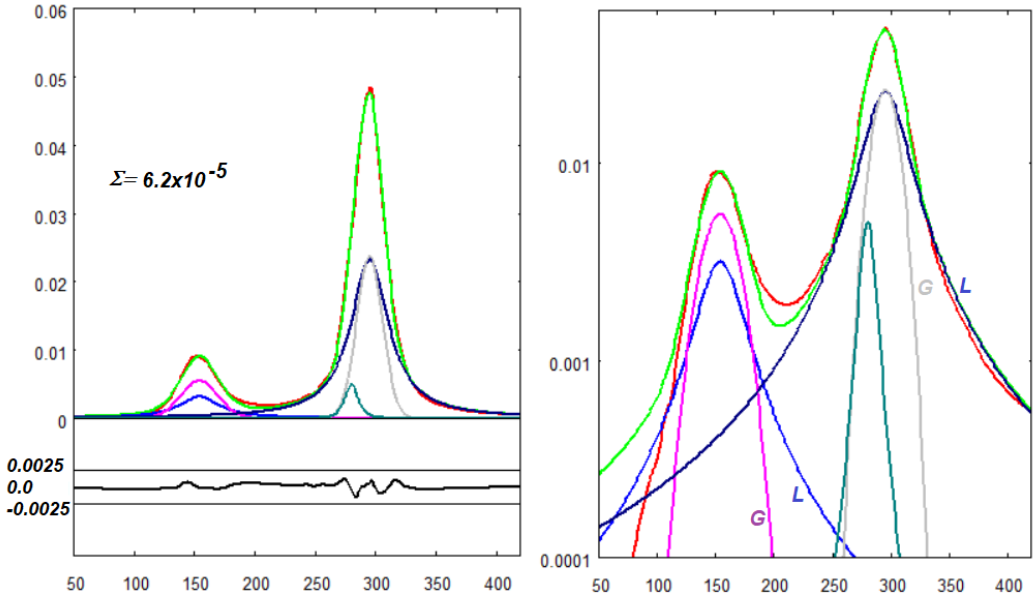

Fig. 11i: Best fit with pseudo-Voigt functions of the first two peaks shown in Fig. 11c. The sum of the squares of the deviations is equal to $6.2x10^{-5}$. Letters G and L are indicating the Gaussian and the Lorentzian components of the pseudo-Voigt function. The third small peak is maintained equal to the q-Gaussian shown in the previous plot. The positions of the center of the components are the same as in the Fig. 9h.

The best fit with the q-Gaussians has a lower sum of the squares of deviations, and this is just due to the shape of the functions. Besides being lower the misfit, an advantage of using the q-Gaussians is in the possibility to give just one FWHM (Full Width at Half Maximum) of the peak (see Appendix A), and not the two values, which are corresponding to the two components of the pseudo-Voigt function.

We could improve the fit by adding components, for instance a component in the valley between the two peaks. Adding this component slightly changes the q-Gaussian components that we can see in the Figure 11i, because it is affecting their tails. This happens for any – let me stress – any line shape we can consider, that is Lorentzian, Gaussian, Voigtian or pseudo-Voigtian, or others. If we add components, we necessarily modify those previously obtained.

Goethite in RRUFF and ROD databases

In the RRUFF database we can find four goethite samples. https://rruff.info/goethite

Here in the following figure, the sample R120086 (chemistry FeO(OH)), source Michael Scott S102426. https://rruff.info/goethite/R120086 .

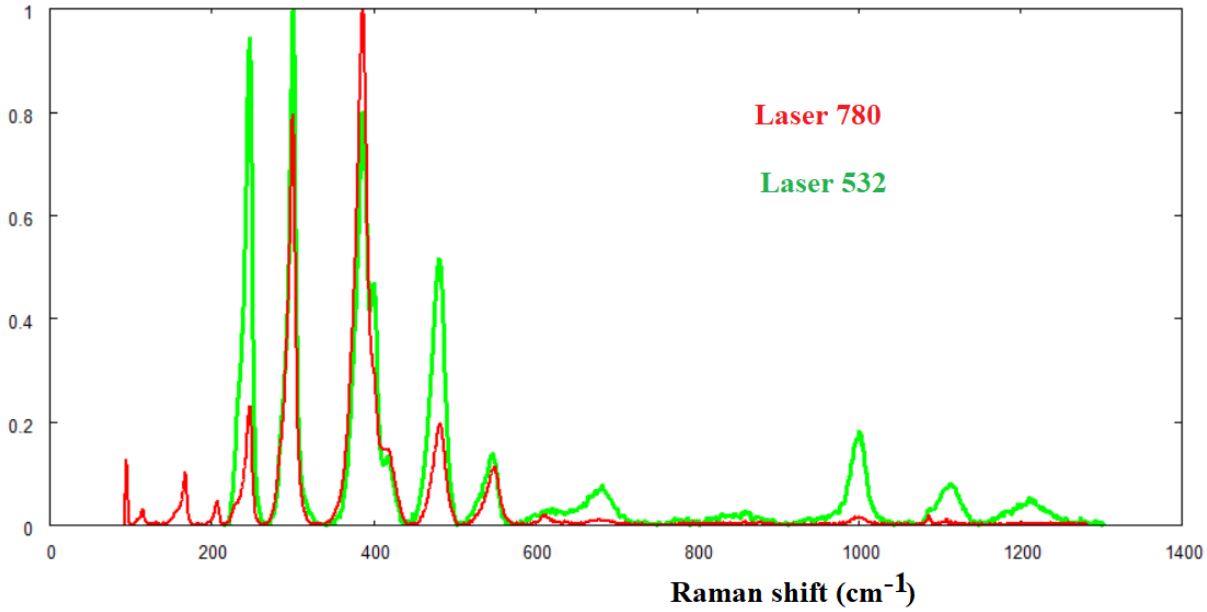

Fig. 12a: Raman spectra of Goethite sample R120086.

Here the peaks from the Raman spectra in RRUFF, compared with the previously give data (in cm^{-1}):

R050142 (laser 532 nm)	*210*	*225*	*246-250*	*302*	*430*			*480*	*550*	*685*	*1000*	*1290*
X050091 (laser 785 nm)		*224*	*245*	*300*	*348*	*388*	*417*	*437*	*478*	*549*		
X050093 (laser 785 nm)			*243*	*298*	*347*	*396*		*438*	*478*	*547*		
R120086 (laser 780 nm)	*....166*		*245*	*300*		*386*			*482*	*549*		
R120086 (laser 532 nm)			*246*	*300*		*387-400*			*481*	*546*		
Thibeau et al.:				*298*		*397*	*414*		*474*	*550*		
Hanesch:			*244*	*299*		*385*			*480*	*548*	*681*	

For R050142 we used the 0° depolarized signal.

In ROD, we can find the Goethite at https://solsa.crystallography.net/rod/3500033.rod and https://solsa.crystallography.net/rod/3500282.rod .

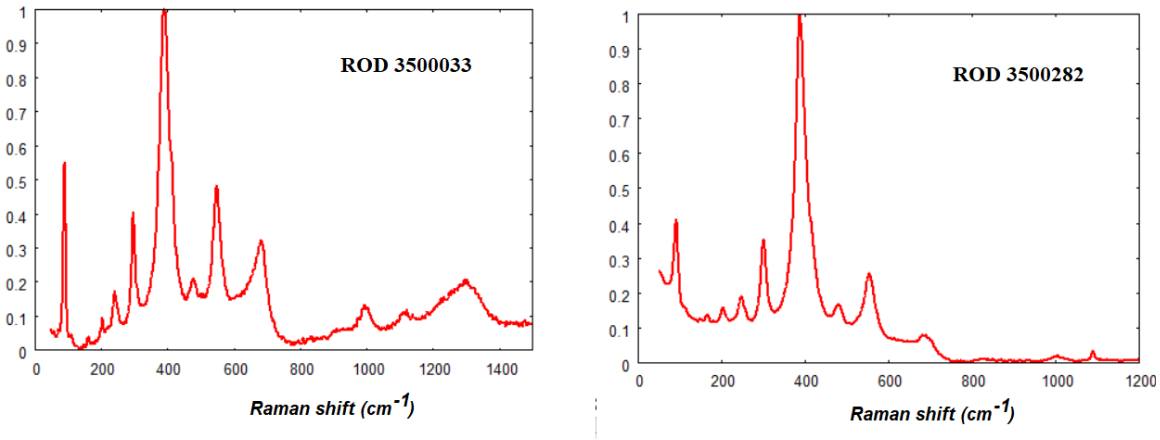

Fig. 12b: Plots Goethite in ROD. On the left, https://solsa.crystallography.net/rod/3500033.rod , El Mendili, Personal communication to ROD, 2017, with the laser excitation wavelength at 532 nm. On the right, https://solsa.crystallography.net/rod/3500282.rod , Kumar et al., Raman spectrum of FeO(OH), with laser excitation at 633 nm.

De Faria et al. studies

The article by De Faria et al. starts observing that "understanding of rusting mechanisms is of fundamental importance in corrosion control". Consequently, "Rust composition has been the subject of several investigations," to understand the corrosion mechanisms. The main corrosion products are oxides and oxyhydroxides, which are strongly absorbing infrared radiation but are poorly scattering light. According De Faria et al., this is a possible reason why we have more studies based on IR spectrometry than on Raman spectroscopy. But Raman spectroscopy has advantages over IR spectroscopy (see them illustrated in De Faria and coworkers' article).

In De Faria et al. we can find stressed that the need for Raman "reference spectra for the most common iron oxidation products [was] inspired [by] the work of Thibeau et al.", who proposed spectra of FeO, Fe_3O_4, α-Fe_2O_3, α-FeOOH and γ-FeOOH. In Hart et al. we can find Hematite and Magnetite, with a "precise and complete assignment" for the bands. Beattie and Gibson studied the effects of orientation for single α-Fe_2O_3 crystals. "Raman spectroscopy was also employed by Boucherit et al., Thierry et al., and Nauer et al., who aimed to characterize corrosion processes in iron-water interfaces". Then, we can find mentioned the SERS studies by Oblonsky and Devine. "In these studies, high laser power was employed (from 100 to 500 mW) and this could lead to sample degradation". With the recent Raman instruments, "it is now possible to obtain good quality spectra even from very poor light scatterers using a few hundred micro watts or even less" (De Faria et al.). The existence of disagreements in the Raman spectra of iron oxides and oxyhydroxides available from literature was the stimulus of De Faria and coworkers' research. We can find Raman spectra of hematite, magnetite, wüstite (FeO), maghemite (γ-F_2O_3), goethite (α-FeOOH), lepidocrocite (γ-FeOOH) and δ-FeOOH. The aim is also that of understanding the influence of laser power.

Hematite

De Faria and coworkers are giving experimental data in the Figures 1-3 of their article. Let us consider their data about Hematite.

Hematite is a crystal with expected seven phonon lines in Raman spectra: two A_{1g} modes (225 and 498 cm^{-1}) and five E_g modes (247, 293, 299, 412 and 613 cm^{-1}). In Hart et al. and R. Beattie and Gilson, the 293 and 299 cm^{-1} bands were resolved at 100 K or less. In De Faria et al., in the Raman spectrum of hematite at room temperature, the 299 cm^{-1} band appears as a shoulder of the 293 cm^{-1} band. De Faria et al. Raman frequencies of Hematite are (in cm^{-1}):

Hematite: 226 245 293 298 413 500 612

Several samples (natural and synthetic hematite) were studied by De Faria and coworkers, finding similar results, "except for changes in relative intensities that occurred when natural samples" had been considered. The researchers explain that the natural samples are much more crystalline than the synthetic samples. Then, the natural crystals are sensitive to sample orientation. Hematite is antiferromagnetic, with magnons as collective spin movements. The intense band at 1320 cm^{-1} is "assigned to a two-magnon scattering". "Raising the laser power to 7 mW (at the sample) causes the bands to broaden and to undergo a small shift to lower wavenumbers".

De Faria and coworkers use as Raman equipment a Renishaw Raman imaging microscope (System 3000) and the spectra are excited with an He-Ne laser 632.8 nm radiation. Here the data (in cm^{-1}):

Laser 0.7 mW: 226.7 245.7 292.5 299. 3 410.9 497.1 611.9

Laser 7 mW: 219.6 236.5 282.7 295.2 395.9 492.3 596.0

(see also Appendix B for the bandshift in graphite).

Let us add the data by Murugappan and coworkers, Monika Hanesch, El Mendili et al., Chamritski and Burns, Owens and Orosz, and Mansour et al. for comparison (in cm^{-1}):

Murugappan et al.:	*205*			*268*			*328*						*560*							
Hanesch:		*225*		*245*		*290-300*			*412*											
De Faria et al.:		*226*		*245*		*293*	*298*		*413*				*500*		*612*					
El Mendili et al.		*229*		*248*		*295*			*414*				*502*		*614*					*1320*
RRUFF 040024	*119*	*225*		*246.5*		*296.5*			*411*				*500*	*558*	*610.5*		*655.5*			*1319*
Chamritski and Burns		*225*		*247*		*293*	*299*		*412*				*498*		*613*					
Owens and Orosz (bulk)		*223*				*288*			*407*	*431*			*493*		*606*		*657*		*711*	
Owens and Orosz (NPs)		*218*				*280*			*394*	*432*			*495*		*602*				*711*	
Mansour et al., Polyol		*224*		*244*		*291*			*408*				*493*		*610*		*659*		*814*	
Mansour et al., Precipitation		*224*		*245*		*293*			*410*				*496*		*613*				*814*	

Let us remember that data by Owens and Orosz have been obtained after the transition to hematite from magnetite induced by the laser power.

In Mansour et al., 2017, it is told that various methods (sol–gel, thermal decomposition, ionic liquid-assisted synthesis, hydrothermal method, co-precipitation method, polyol) exist to prepare α-Fe_2O_3 nanoparticles. Moreover, hematite particles were also prepared by means of the precipitation of β-FeOOH. Mansour and coworkers used two methods: (1) polyol and (2) precipitation in water. "The

influence of synthesis methods on the crystalline structure, morphological, optical, magnetic and electrical properties were investigated", using the Raman spectroscopy too. In the Figure 3 by Mansour et al., we can find the peaks as given in the previous page.

Encapsulating Iron Oxide (IronOxide@C)

We have mentioned before the encapsulation of magnetic nanoparticle. Let us consider here an article which is containing the mechanism of reduction.

In Song et al., 2012, an approach to an "amorphous carbon coating on the surface" of iron oxide particles, "via a simple glucose treatment" is given. The researchers obtained "novel configurations of iron oxides [which] possess an amorphous carbon layer and ferrous state with high electronic conductivity, which definitely enhances their electrochemical properties compared to pristine iron oxides". In the Figure 4 by Song et al., we can find "the Raman spectra of iron oxide and carbon-encapsulated Fe_3O_4 nanocrystals. Iron oxide can normally be categorized as a material for which special care has to be taken during the measurement of Raman spectra because the transition metal (iron) inside its structure is divalent (ferrous or ferric)". Song and coworkers tell that the Raman spectrum of the pristine iron oxide that they have characterized possesses three broad bands at 390, 590 and 710 cm^{-1} and two bands around 1360 and 1580 cm^{-1} attributed to a typical hematite" (Song et al., mentioning Shebanova and Lazor). Song et al. do not provide information about the used Raman equipment and laser power.

Song and coworkers continue in the following manner. "Because a laser with even very low energy can evolve numerous spurious peaks attributed to hematite in the Raman spectra of magnetite, the peaks at 300 and 410–420 cm^{-1} also reported in some previous studies on magnetite are relevant to an oxidation reaction during a Raman experiment". Song and coworkers are giving details about the magnetite Raman bands, which the authors are indicating in their Figure 4. Using glucose to prepare the nanoparticles, the researchers "figure out that the glucose treatment is definitely *relevant to the phase transition from hematite to magnetite* [Graves et al., Varadwaj et al., 2004]. … there is a clear change associated with the turnaround of intensity between the D band (1350 cm^{-1}) and the G band (1580 cm^{-1}) after the decomposition of glucose. The augmented D band compared to the G band shows us that *the decomposition of glucose not only activates the phase transition of hematite to magnetite* but also makes the amorphous carbon layer on the surface of the evolved magnetite iron oxide show good agreement with XRD and TEM results" (Song et al., 2012). From hematite to magnetite? See Ponomar, 2018, and the discussion of magnetite prepared by chemical reduction from hematite. In Ponomar et al., 2017, the use of carbohydrates in the reduction roasting of hematite to magnetite is discussed.

When discussing the XPS spectrum (XPS; X-ray photoelectron spectroscopy), Song and coworkers are telling that "In Fe 2p spectra, the reduction of Fe^{3+} to $^{Fe2+}$ is prominent; this is induced by the increase of C=O and O–C=O bonding" (Song et al., 2012). "Moreover, the atomic contents obtained in the Fe 2p spectra reveal that the pristine iron oxide is composed of α-Fe_2O_3 [hematite] or γ-Fe_2O_3. [maghemite]. But after the glucose treatment on iron oxide, the ratio (33 at.%: 67 at.%) between Fe^{2+} and Fe^{3+} accords very well with the theoretical stoichiometry of Fe_3O_4, probably due to the carbothermal reaction associated with glucose treatment" (Song et al., 2012). As explained by Song and coworkers, "C and H can act as oxygen getters during the decomposition of glucose because most of C and H from glucose ($C_6H_{12}O_6$) preferentially tend to react with oxygen, as a result reducing the oxygen content in the pristine iron oxide".

Here the Raman peaks of IronOxide@C (Song et al., in cm^{-1}):

225 284 334 389 506 582 713 1176 1392 1605

In Song et al., 2012, we have found that magnetite nanoparticles can be obtained by reduction from amorphous iron oxide, or as told in the article, by means of a transition "from hematite to magnetite", assisted by glucose. For glucose coated Fe_3O_4 nanoparticle, see Sun et al., 2009.

Actually, Fe_3O_4@C nanoparticles have been obtained by Xuan et al. in 2007, for the first time with one-step hydrothermal carbonization: "to the best of [Xuan and coworkers'] knowledge, there has been no report about the fabrication of Fe_3O_4@C core/shell composites via a one-step hydrothermal carbonization coreduction technique under such [given by Xuan and coworkers] temperatures". The synthesis is described as follows. Glucose, $FeCl_3$ and urea were dissolved in water under stirring vigorously; then solution has been sealed in Teflon-sealed autoclave. "The autoclave was kept at 180 °C for 14 h before been cooled naturally". The magnetic particles were separated magnetically and dried. XRD tells that nanoparticles are made of magnetite. The Raman spectrum is provided in the Figure 2 by Xuan and coworkers; the Raman shift starts from 500 cm^{-1} and therefore we have not the part of the spectrum which could indicate a laser induced oxidation. But, in the given spectrum we can see an interesting low and broad peak at about 700 cm^{-1}. The same bump is visible in the Figure 4 by Song et al., 2012.

"The magnetic properties of the product were examined using a Quantum Design SQUID magnetometer at room temperature (figure 8 [in Xuan et al., 2007]). As shown from the magnetic hysteresis loop, the products exhibit typical ferromagnetic curves, with a saturation magnetization of 41.6 emu g^{-1}. Taking into account that the sample contains 74% Fe_3O_4, this gives a value of 56.2 emu g^{-1}. This value is much lower than that of the corresponding bulk Fe_3O_4 (92 emu g^{-1})" (Xuan et al., mentioning Han et al., 1994). This "may be due to the amorphous carbon shell", with a consequent "disordered structure at interfaces providing less magnetic moment per unit mass than that of ferromagnetic core regions"; the disorder is leading "to a decrease in the M_s" (Xuan et al., mentioning Tamura and Endo, 1969). Let us remember that 1 emu/g = 1 Am^2/kg and 1 Oe = 79.57747 A/m. Then 1000 Oe are equal to 79.577 kA/m.

As explained by Nguyen et al., 2021, "Fe_3O_4 has attracted more attention than other iron oxides or ferrite spinel oxides (MFe_2O_4 with M = Co, Ni, Mg, etc.) because of its superior magnetic properties, electronic conductivity, and biocompatibility". We can explain the magnetism of magnetite with its crystal structure. "Magnetite has a cubic inverse spinel crystal structure consisting of Fe^{2+} cations occupying 25% of the octahedral interstitial sites and Fe^{3+} cations occupying 25% of the octahedral sites and 12.5% of the tetrahedral sites, and thirty-two O^{2-} anions in its unit cell" (Ngyen et al., and references therein). Nguyen and coworkers continue clearly explaining that "The magnetic moments of Fe^{3+} and Fe^{2+} cations in octahedral holes are coupled ferromagnetically. However, the Fe^{3+} ions in tetrahedral sites possess magnetic dipoles in the reverse direction of the Fe^{3+} ions in the octahedral sites. Therefore, Fe_3O_4 is a ferrimagnetic material with high saturation magnetization (M_S) and low coercivity (H_C) due to the antiferromagnetically coupled Fe^{3+} cations in tetrahedral and octahedral sites of its crystal structure" (Nguyen et al., 2021). Nguyen and coworkers are also stressing: "the term ferromagnetic properties or ferromagnetism is [sometimes] also used for Fe_3O_4, which indicates that it exhibits magnetic properties in the absence of a magnetic field" (Nguyen et al., 2021). In fact, we can find in Xuan et al. the "ferromagnetic core" of the nanoparticles. Nguyen and coworkers are also providing data about maghemite, ferrimagnetic material, and hematite, weak ferromagnetic material. "The maximum values of saturation magnetization (M_S) for magnetite (Fe_3O_4) and maghemite (γ-Fe_2O_3) are 98 emu/g and 82 emu/g, respectively (Nguyen et al., mentioning Colombo et al., 2012), whereas the values for saturation magnetization of hematite (α-Fe2O3) are usually modest and reported to be approximately 2 to 4 emu/g" (Nguyen et al., and references therein). "In the case of spinel ferrite MFe_2O_4, the maximum saturation magnetization values for $CoFe_2O_4$, $NiFe_2O_4$, and $MgFe_2O_4$ are 94 emu/g, 56 emu/g, and 31 emu/g, respectively" (Nguyen et al., mentioning Colombo et al., 2012).

Akaganeite and Siderite

We have seen that glucose can be used for obtaining the nanoparticles. Here it is therefore worthwhile to mention biological processes. In Lee et al., 2003, we can find the "formation of Fe(II)-containing mineral through microbial processes". This formation "may play an important role in iron and carbon geochemistry in subsurface environments. Fe(III)-reducing bacteria form Fe(II)-containing minerals such as siderite, magnetite, vivianite, and green rust using iron oxides" (Lee at al., 2003). Lee and coworkers, in their article, are proposing the "biomineralization" of akaganeite, which is a "poorly crystalline Fe(III) oxide", by means of "an anaerobic Fe(III)-reducing bacterium (Shewanella alga) isolated from marine environment" (Lee et al., 2003).

In Cornell and Schwertmann, 2003, Akaganeite is indicates as β-FeOOH. It is named after the Akagane mine in Japan and first described in 1962. Rare in nature, it is occurring in Cl-rich environments and in marine environments. In the Handbook of mineralogy (Anthony et al., 2001), the formula is given as β–$Fe^{3+}O(OH, Cl)$.

We have the occasion to show the Raman spectrum of Akageneite provided by ROD database.

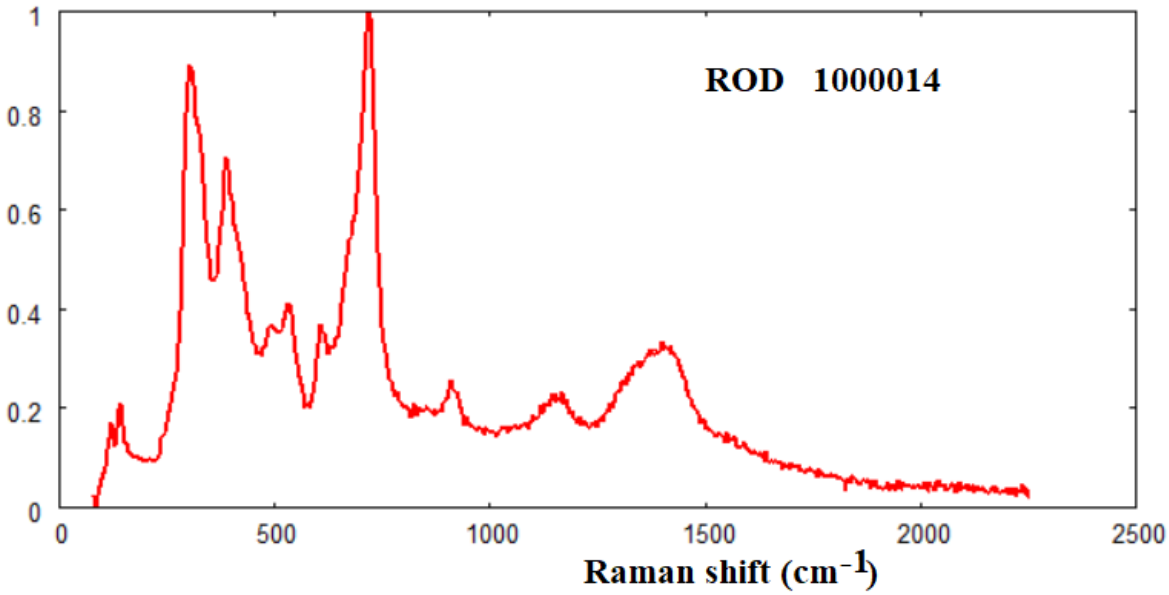

Fig.13: Akaganeite Raman spectrum available at https://solsa.crystallography.net/rod/1000014.rod by El Mendili et al., 2014.

Monika Hanesch is also proposing the Siderite Raman spectrum, telling that it is "easy to obtain as the mineral is stable at moderate laser power". The bands that Hanesch has evidenced are coincident with "published siderite bands (e.g. Rull et al. 2004) at 184, 287, 731 and 1090 cm^{-1}". The chemical systematic name of Siderite is iron(II) carbonate.

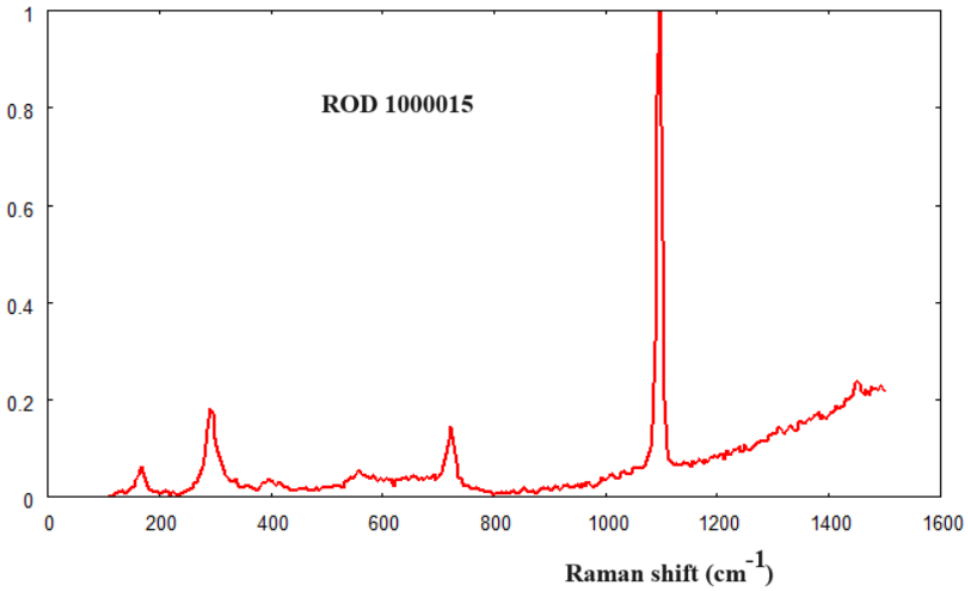

Fig.14: Siderite Raman spectrum available at https://solsa.crystallography.net/rod/1000015.rod by El Mendili et al., 2014.

Peaks are at (in cm^{-1}):

ROD Siderite: 168 291.5 394.5 556 724 1097

For the interpretation of the Raman spectrum of Siderite, see please the database by Buzgar N., Apopei A. I., Buzatu A., 2009, Romanian Database of Raman Spectroscopy (http://rdrs.ro), at the following link http://www.rdrs.ro/minerals/carbonates/anhydrous-carbonates/siderite-raman-spectrum/ . It is told that the Siderite Raman spectrum is "characterized by the same band of calcite", which is "corresponding to the symmetric stretching of CO_3 group". The two bands at low Raman shift values are due to T(Fe, CO_3) mode.

Maghemite NPs capped with polyol

In Varadwaj et al., 2004, we find maghemite (γ-Fe_2O_3, about maghemite see also Bahari, A. (2017). "Among the various magnetic nanomaterials, γ-Fe_2O_3 is used in magnetic memory devices, color imaging, magnetic refrigeration, ferrofluids, catalysis and sensors. Coating or capping[2] the nanoparticles with polymers or organic moieties further enhances their applicability as it prevents agglomeration and the material becomes dispersible in aqueous or organic solvents" (see please Varadwaj et al., and

[2] Capping agents are amphiphilic molecules. The molecules have polar heads and nonpolar hydrocarbon tails. "The functionality of the capping agent depends upon both the parts. The non-polar tail interacts with surrounding medium whereas polar head coordinates to the metal atom of the nanocrystals." (Gulati, et al., 2018).

references therein). Varadwaj and coworkers propose γ-Fe_2O_3 "nanoparticles capped with a polyol", "synthesized by a one- step method". Stability towards degradation is investigated with Raman laser.

Varadway and coworkers used a Renishaw Raman System 1000B and a laser at 514 nm. "Most of the Raman studies on bulk iron oxides have been on Fe_3O_4 and α-Fe_2O_3". In magnetite we have five Raman bands, but in "earlier studies only four bands at 193, 306, 538 and 668 cm^{-1} are observed" (Varadway et al., mentioning Shebanova and Lazor). For α-Fe_2O_3, seven "phonon lines are expected at 225, 247, 293, 299, 412, 498 and 613 cm^{-1}. In addition to these bands an intense band at 1320 cm^{-1} is observed due to a two magnon scattering". The γ-Fe_2O_3 has a Raman spectrum characterized by three broad bands around 350, 500 and 700 cm^{-1}, not present in the spectrum of any iron oxide or oxyhydroxide.

Green and hydrothermal synthesis routes to Fe_3O_4 nanoparticles

In De Jesús Ruíz-Baltazar et al., 2019, we can find proposed the green synthesis of Fe_3O_4 nanoparticles by means of the *cynara cardunculus leaf extract*. This synthesis route, which is considered as a green synthesis route, is defined as a "co-friendly alternative to obtaining of iron oxides nanoparticles" (De Jesús Ruíz-Baltazar et al., 2019). According to De Jesús Ruíz-Baltazar and coworkers, "the Fe_3O_4 nanostructures were synthesis starting [from] a mixture of ferric chloride and ferrous chloride in a 1:2 M ratio. The reducing agent employed was cynara cardunculus leaf extract". These nanoparticles are proposed for "water remediation containing organic dyes". The researchers characterized the particles by means of scanning electron microscopy (SEM) and X-ray diffraction (XRD), among other techniques. And the Raman spectroscopy has been used to support the characterization of magnetite nanoparticles. The prepared nanoparticles have been "evaluated on the methylene blue degradation".

In Figure 4 by De Jesús Ruíz-Baltazar et al., 2019, we can find the Raman spectrum (no information about instrumentation and laser line and power). The peaks that we can observe are (in cm^{-1}):

Magnetite (M) and Hematite (H)	*221*	*302*	*401*	*499*	*545*	*604*	*667*
	H	*M*	*H*	*H*	*M*	*H*	*M*

The letters under the peaks are the assignment by De Jesús Ruíz-Baltazar and coworkers. "Additionally, the band associated to the magnetite and hematite phases are corroborated with Raman spectra obtained from the RRUFF Raman Mineral Spectra database (University of Arizona)". It "Is important to note that the magnetite and hematite phases are presents in the experimental Raman spectrum, however, the majority phase observed is the magnetite" (De Jesús Ruíz-Baltazar et al., 2019).

In Ni et al., 2009, the hydrothermal synthesis of magnetite nanoparticles, to be used in lithium-ion batteries, is exposed. "All the chemicals were of analytical grade and purchased from Shanghai Chemical Reagents. In a typical procedure, 5 mmol $(NH_4)_2Fe(SO_4)_2{\cdot}6H2O$, 2.5 mmol hexamethylenetetramine, and 1 g sodium sulfate were dissolved in 30 ml distilled water. After stirring for 20 min, the homogeneous green solution was transferred into a 50 ml Teflon lined autoclave, … The autoclave was sealed and placed in an oven, heated at 90 °C for 24 h. After the reaction, the autoclave was cooled in air. The suspension was washed … and the resulting black precipitates finally were dried in an oven at 60 °C for 24 h" (Ni et al., 2009). A Micro-Raman spectrometer (Jobin Yvon LabRAM HR800 UV, YGA 532 nm) was used.

"Raman spectra in the wavelength range of 150–1200 cm^{-1} were dominated by three peaks located at 318, 517, and 671 cm^{-1}" (Ni et al., 2009).

Ferric Nitrate, Biochar and Fe_xO_y particles

In ChemRxiv, January 2023, we considered the literature regarding the use of Fe_3O_4 nanoparticles for EMI shielding. From this work we can deduce that, besides the use of encapsulated NPs to have composites, another approach is that of mixing the precursors of magnetic nanoparticles directly in a relevant supporting material. In the ChemRxiv article, we also focused on biochar as support of NPs. In "the catcher in the water", we further discussed that the magnetic biochar[3] can be obtained from the same raw materials used to have biochar. With the inclusion of iron or addition of magnetic precursors, biochar turns into a material which has magnetic separation capabilities. It is used for the treatment of wastewater pollution, such as removing heavy metals, nuclear and organic pollutants. After the treatment of water, the magnetic biochar which has collected the pollutants, can be easily removed from water by a magnetic field.

About precursors and biochar, in ChemRxiv we reported that Li et al., 2016, proposed a Fe_3O_4@Biochar obtained as follow. The spongy pomelo pericarp is used for biochar, grounded into fine powders. Biochar is mixed with $Fe(NO_3)_3.9H_2O$ (ferric nitrate also known as iron nitrate) in water. After intense stirring, the mixture is desiccated and dried. Put into a tube furnace and heated in flowing N_2, the final product is denoted as Fe_3O_4 NP/C (see all details in the article by Li et al., 2016, and also how the prepared biochar is acid-treated). In Li et al., 2016, we cannot find Raman spectra. Raman spectra are given in Nguyen et al., 2020, where the magnetic Fe_3O_4 nanoparticles are decorating biochar obtained from pomelo peel. The researchers prepare different mixtures, one of them is named FO5 (Fe Oxide n.5). Nguyen and coworkers tell that "to confirm the composite formation between Fe_3O_4 and PPB [pomelo peel biochar], Raman spectra was measured at an excitation wavelength of 635 nm using a Renishaw spectrometer. Figure 4(c) [in Nguyen et al.] shows Raman spectra of PPB, Fe_3O_4 nanoparticles, and FO5-PPB before and after adsorption". No information about the laser power is provided and no mention of the related oxidation problems. "The whole spectra displayed almost all the peaks that are characteristic to the Fe_3O_4 magnetite structure and graphite of carbon materials. Peaks at lower Raman shift values (218, 276, 393, 687, and 698 cm^{-1}) … may indicate the vibration modes of Fe–O bonds within each Fe_3O_4 nanoparticle and the Fe–C bonds on the surface of the PPB" (Nguyen et al., mentioning Tiwari et al., 2007 and 2008). As told before, Tiwari and coworkers have not studied carbon, therefore they are not mentioning Fe-C at the surface of biochar (see the Appendix about Tiwari et al. works). In any case, here the peaks provided by Nguyen et al. for FO5 (in cm^{-1}):

FO5: 218 276 398 485 594 1298

(see please the Raman shift of the peaks given previously in the discussion about the laser power and the debris fingerprint).

We can find some information about Fe-C interaction in Chen et al., where a "facile fabrication of 3D biochar absorbers dual-loaded with Fe_3O_4 nanoparticles for enhanced microwave absorption" is proposed. The Raman spectra are given for the Fe_3O_4@SP[spirulina]-BC and SP-BC composites (Fig. 2b [of Chen et al.]). Chen and coworkers are not showing the Raman shift below 300 cm^{-1}. "All the samples exhibited two characteristic peaks at approximately 1340 cm^{-1} and 1585 cm^{-1}, which represented effective carbonization in the form of D and G bands, respectively" (Chen et al., 2023). "Generally, the I_D/I_G ratio [I intensity] is commonly utilized to assess the defects and disorder degree in carbonized composites. In this case, the I_D/I_G value of Fe_3O_4@SP-BCs was higher than that of SP-BC-

[3] Biochar is the black residue, composed of carbon and ashes, obtained after the pyrolysis of biomass. According to the International Biochar Initiative, biochar is "the solid material obtained from the thermochemical conversion of biomass in an oxygen-limited environment".

700, indicating that more defects and disordered carbon components were formed due to the loading of Fe_3O_4 NPs" (Chen et al., 2023).

According to Chen and coworkers, the composite is characterized by a "strong dipole polarization in the biochar matrix under EM waves, which further enhanced the dielectric loss of the absorbers" (Chen et al., and references therein). "The I_D/I_G ratio increased distinctly as the carbonization temperature increased", and this "could be attributed to the complete pyrolysis of organic components in the Fe_3O_4@SP precursors" (Chen et al., 2023). In Gong et al., 2022, where Fe_xO_y@Biochar composite materials are studied for high-efficiency microwave absorption, we can find an analysis of the I_D/I_G ratio too. Being the analysis regarding the D and G peaks, the Raman spectra are not shown below 500 cm^{-1}.

Gong and coworkers selected the almond shells and ferric nitrate to prepare the composites. The Fe_xO_y@Biochar was prepared with the heat treatment of almond shells in different concentrations of iron nitrate solution at 600, 800 and 1000 °C, respectively. "The composite material was examined and found to have good microwave absorption properties and multi-loss synergistic effects". "Therefore, almond wood porous biomass carbon exhibits strong microwave absorbing properties" (Gong et al., 2022). "At high temperatures, carbon reduces iron nitrate to form a mixture of iron oxide, ferroferric oxide, and iron". In the Table 2, provided by Gong et al., we can find the iron-containing substances produced by the reaction at temperatures above 500 °C. For the temperature range 500-600 °C, the solid residues are of $Fe(NO_3)_3$, Fe_2O_3, Fe_3O_4. For 600-800 °C, the residues contain Fe_2O_3, Fe_3O_4, Fe. Iron (Fe) is the residue for the range 800-1000 °C.

In Srivastava et al., 2010, an investigation on magnetic properties of α-Fe_2O_3 NPs "synthesized under surfactant-free condition by hydrothermal process" was proposed. Two different precursors, $FeCl_3$.6H2O and $Fe(NO_3)_3$.$9H_2O$ have been used. Srivastava and coworkers used X-ray diffraction (XRD), Raman spectroscopy (RS), microscope (SEM and HR-TEM), and vibrating sample magnetometer (VSM). The average particle size of the nanoparticles synthesized with the two precursors is different. The magnetic properties of the nanoparticles are different too, because of the different size. The Raman peaks are (in cm^{-1}):

From Ferric Nitrate	*220*	*286*	*399*	*491*	*602*
From Ferric Chloride	*220*	*286*	*399*	*488*	*597*

In Bagherzadeh et al., 2023, we can find the "preparation of Fe_3O_4/vine shoots derived activated carbon nanocomposite" to be used for removal of Cr (VI). This is a reference which is interesting for the proposed magnetic investigation. "According to the VSM [Vibrating-Sample Magnetometer] … it can be seen that the maximum magnetization of Fe_3O_4 is higher than Fe_3O_4/C nanocomposites, which is due to non-magnetic nature of the activated carbon. … However, the magnetic property of Fe_3O_4/C is strong enough that it can to be quickly separated from the heavy metal ion solution using an external magnetic field" (Bagherzadeh et al., 2023). Experiment tells that "both samples are superparamagnetic; also composite saturation magnetization of 30.34 emu g^{-1}, gives the adsorbent the privilege of magnetic separation and good retrievability" (Bagherzadeh et al., 2023).

Red mud

Red mud is defined as "a hazardous waste material produced during the alkaline leaching of bauxite in the Bayer process" (Tang et al., 2022). The red mud is made of "coarse sand and fine particle. Its composition, property and phase vary with the type of the bauxite and the alumina production process, and will change over time" (Wang and Liu, 2012). Wang and Liu are also providing the chemical components, as in the following Table.

Main chemical components	Fe_2O_3	Al_2O_3	SiO_2	CaO	Na_2O	TiO_2
Bayer process	26.41	18.94	8.52	21.84	4.75	7.40
Sintering process	7.95	10.36	17.29	40.22	3.53	7.14

A question could be: are we able to evidence with Raman spectroscopy the presence of the iron oxides in the red mud? Let us consider literature.

In He et al., 2020, we can find a study of Arsenic (III) removal by means of the formation of ferric arsenite. The composition of the used red mud is Fe_2O_3 33.1%, Al_2O_3 20.57%, SiO_2 15.10%, CaO 2.10%, Na_2O 9.79% and TiO_2 5.77%. The Raman peaks of the original red mud are (in cm^{-1}):

Original Red Mud	*132*	*210*	*274*	*400*	*693*	*1287*
		Fe-O	*Fe-O*	*Al-O*	*Si-O*	*H_2O*

"The Bayer process is the primary method by which alumina (Al_2O_3) is produced from bauxite ore. In this hydrometallurgical process, caustic soda digestion under elevated temperature and pressure is used to leach soluble alumina minerals from the bauxite ore and subsequently precipitate technically pure aluminum hydroxide. From the pregnant leach solution, the residual mineral matrix is removed as a byproduct, commonly termed as bauxite residue or *red mud*" (Vind et al., 2018). Vind and coworkers have performed μ-Raman spectroscopy, using a Renishaw inVia confocal Raman microscope, 785-nm laser "at a power of 25–50 mW at laser source". The hematite-dominant particles of bauxite residue have been reported as 170 mg/kg. "In the bauxite residue sample, another iron phase was distinguished from hematite" thanks to "its darker hue in the backscattered electron imaging mode". It is the iron oxyhydroxide of the goethite "in μ-Raman spectroscopic analysis (bands 204, 221, 240, 296, 396, 472, 546 cm^{-1})" (Vind et al., 2018). According to the area investigated, the peaks are (in cm^{-1}):

Hematite area as in Figure 3 in Vind et al.			*225*	*245*	*292*	*411*	*450*	*496*	*610*	*661*
							Diaspore?			*Magnetite?*
Goethite area as in Figure 6a in Vind et al.	*204*	*221*	*240*	*296*	*396*		*472*	*546*	*609*	*682*
									Hematite?	*Magnetite?*
Hematite area as in Figure 6b in Vind et al.			*224*	*246*	*291*	*410*	*450*	*495*	*609*	*676*
							Diaspore?			*Magnetite?*

"The red mud exhibits the presence of hematite (Fe_2O_3), alumina (Al_2O_3), gibbsite ($Al(OH)_3$) quartz (SiO_2), anatase and rutile (TiO_2) and calcite ($CaCO_3$)" (Kumar et al., 2020, mentioning Liu et al., 2009). "The Raman results for red mud are shown in Fig. 2(d) [by Kumar et al.]. The various broad peaks at the same wavenumber are responsible for different metal oxides in red mud. Due to a large amount of hematite (Fe_2O_3) in red mud, [we can see] four dominating peaks at 211, 275, 387, 620 cm^{-1}" (Kumar et al., 2020). "The peak at 150 and 508 cm^{-1} are due to anatase (TiO_2) and quartz (SiO_2) respectively" (Kumar et al. mentioning Palmer & Frost, 2009).

Remarks

After the examined literature, we can remark that:

1) It is convenient to use filters to reduce laser power to avoid the sample deterioration.
2) Time is also important, to understand how sample oxidation is evolving.
3) Encapsulation seems being important to maintain the superparamagnetic nature of Fe_3O_4.
4) XRD is distinguishing magnetite and hematite.

Appendix A – q-Gaussian Tsallis functions

The q-Gaussian functions are probability distributions proper of the Tsallis statistics (Tsallis, 1988, Hanel et al., 2009). These functions are based on a generalized form of the exponential function (Sparavigna, 2022), where a continuous real parameter q is characterizing it. When q is going to 1, the q-exponential becomes the usual exponential function. The value q=2, (Naudts, 2009), corresponds to the Cauchy distribution, also known as the Lorentzian distribution; then, the q-Gaussian function is a generalization of the Lorentzian distribution too. The change of q-parameter is therefore allowing the q-Gaussian function to pass from the Gaussian to the Lorentzian distribution.

The Raman spectroscopy bands are usually given as characterized by Lorentzian or Gaussian distributions, or by a *linear combination* (pseudo-Voigt distribution) or by the *convolution* of them (Voigt distribution) (Meier, 2005). In previous works (Sparavigna, 2023), we have shown that q-Gaussians are properly mimicking pseudo-Voigt, Voigt functions and the Egelstaff-Schofield spectral line shapes. We have also discussed in detail the Raman spectroscopy, for what is regarding the D and G bands of carbon-based materials[4].

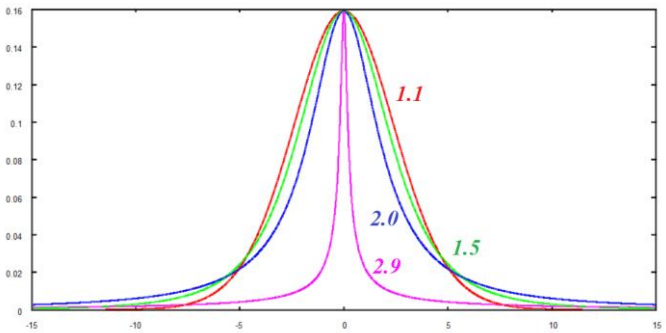

Fig. A.1: q-Gaussian functions, for different q indices, from 1.1 (quasi-Gaussian) to 2.9 (over-Lorentzian). The blue curve is the Lorentzian line shape.

As given by Umarov et al., 2008, the q-Gaussian function is:

$$f(x) = Ce_q(-\beta x^2),$$

where $e_q(.)$ is the q-exponential function and C a scale constant. In the exponent, we use $\beta = 1/(2\sigma^2)$.

The q-exponential has the expression:

$$exp_q(u) = [1 + (1-q)u]^{1/(1-q)}.$$

4 See discussion in https://papers.ssrn.com/sol3/papers.cfm?abstract_id=4445044 . The G-band is the main Raman mode in graphite and graphene, linked to the planar configuration sp^2 bonded carbon, which is constituting the graphene layers. The D-band is the "disorder band" or the "defect band", and it is related to the ring breathing mode from sp^2 carbon rings. If this D-band is significant, it means that defects are present in the material.

The plots in the Figures A.1, A.2 and A.3 are showing the behaviour of this exponential for different q values. Note that, for q less than one, the function is different from zero on a limited interval.

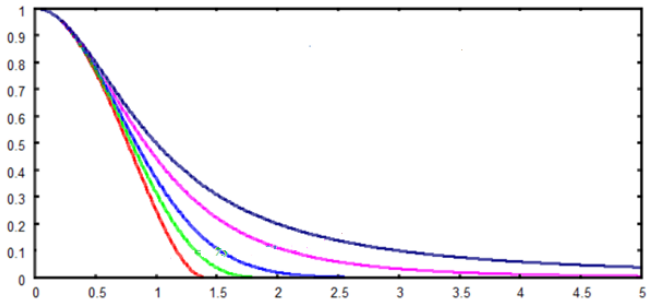

Fig.A.2: q- exponential functions, where the blue curve is representing a Lorentzian function (q=2). The pink curve corresponds to q=1.5 and light blue to q= 1.01, practically a Gaussian function. The green curve is the q-Gaussian for q=0.75 and red curve for q=0.5. For q < 1, the function is different from zero in a limited interval. Being the line symmetric, only the right part of it is given in the figure.

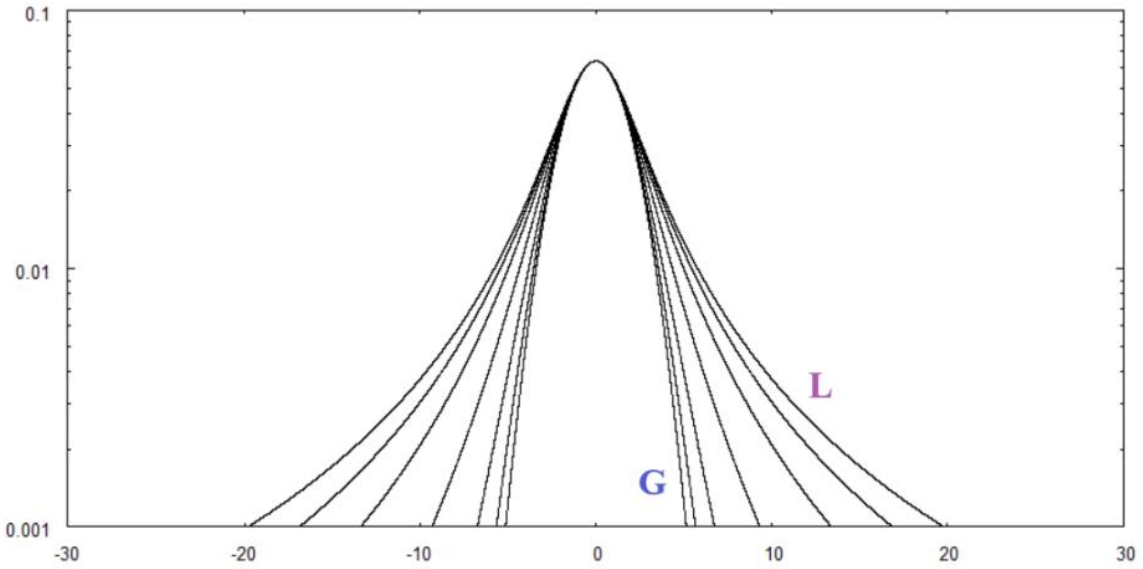

Fig.A.3: q-Gaussians, between the Lorentzian L and the Gaussian G function, in a log scale for the y-axis.

The Half Width at Half Maximum of q line shape is given by: $\sqrt{2}\,\sigma\,\sqrt{(1-(1/2)^{1-q})/(1-q)}$.

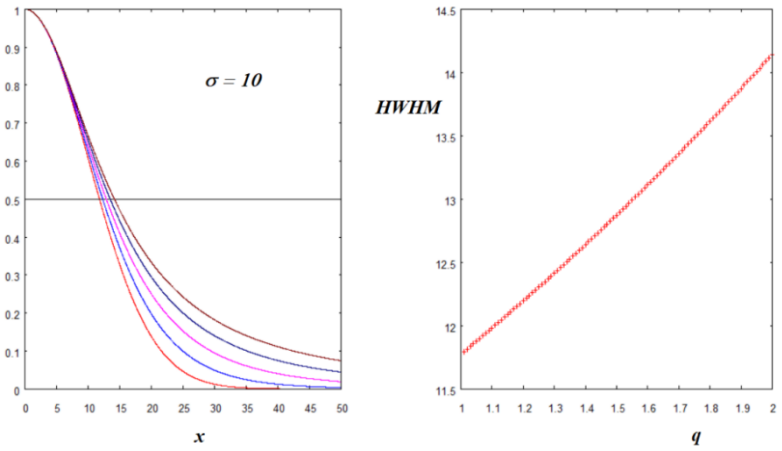

Fig.A.4: q- exponential functions for q=1.01 (red), 1.25, 1.50, 1.75 and 2 on the left; on the right, the Half Width at Half Maximum as a function of q.

A recent publication (published on May 18, 2023) by V. Witkovský is telling that "The Tsallis q-Gaussian distribution is a flexible and versatile generalization of the standard Gaussian distribution that can effectively model input quantities in a wide range of applications and measurement models". Mentioning Vignat and Plastino, 2009, Witkovský considers "the possible reasons why q-Gaussian distributions are frequently observed in various natural and artificial phenomena. They [Vignat and Plastino] argue that the detection of q-Gaussian behavior may be influenced by the normalization process performed by the measurement device".

Appendix B – Bandshift induced by laser

Let us here stress the existence of the bandshift induced by laser as given by Everall, et al., 1991. In the Figure 1 of their work, we can find depicted the "laser-induced bandshift in single (40 μm diameter) graphite grains: (a) E_{2g} mode, 1 mW laser beam power at sample. (b) E_{2g} mode, 6 mW laser beam power. The original band position was restored on returning the laser power to 1 mW". Everall and coworkers told that "the likely explanation for these effects is that localised sample heating occurs and distorts the vibrational spectrum, although a simple interpretation in terms of expansion of the graphite lattice parallel to the layers cannot hold, since the in-plane coefficient of thermal expansion is negative below 400 °C." In the following figure, on the left, it is given the analysis of obtained with 1 mW beam power, on the right that for the 6 mW case. The peak is fitted by a q-Gaussian (see pag.50 of article available SSRN).

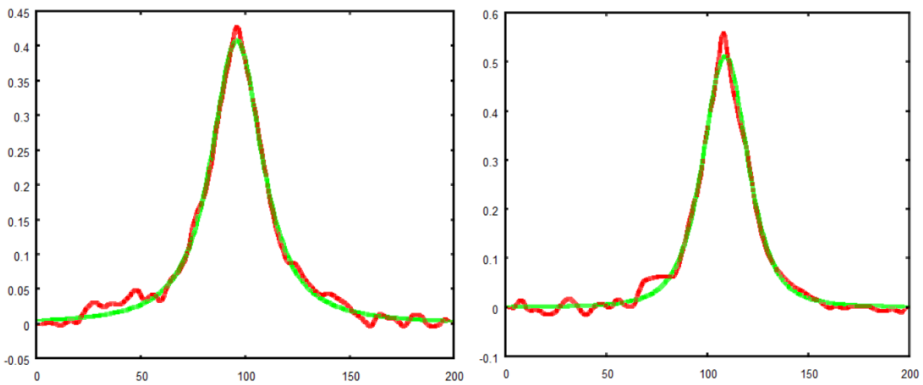

Fig. B.1: Data (red) and best fit (green) of the Raman spectra in the Figure 1 by Everall et al., 1991. On the left, the peak is given at 1575 cm^{-1}, the beam power was of 1mW; on the right (1565 cm^{-1}) the power was of 6 mW. The q-parameters of the best fit are different. On the left, q=1.78, on the right q=1.48 .

Appendix C – Magnetic properties of Iron oxides

In Cornell and Schwertmann, 2003, we can find the magnetic structure and the properties of iron oxides. Here we report only the temperatures (T_N = Néel temperature, T_C = Curie temperature, T_M = temperature of Morin transition, in Kelvin), and the magnetic structures.

Oxide - Temperature - Magnetic structure

Goethite - 400 T_N -- antiferromagnetic

Lepidocrocite - 77 T_N - antiferromagnetic

Akaganéite - 290 T_N - antiferromagnetic

Delta-FeOOH - 440-460 T_N - ferrimagnetic

Feroxyhyte - 459 T_C - ferrimagnetic

HP FeOOH .. about 350 T_N - antiferromagnetic (HP high pressure)

Ferrihydrite - about 350 T_N - speromagnetic

Bernalite - about 427 T_N - weakly ferromagnetic

Hematite - 956 T_C - weakly ferromagnetic

Hematite - 260 T_M - antiferromagnetic

Magnetite - 850 T_C (T_N in Kozlenko et al., 2019). - ferrimagnetic

Magnetite - 120 Verwey transition - ferrimagnetic

Maghemite - 820-986 T_C - ferrimagnetic

Epsilon-Fe_2O_3 - 1016 T_N - antiferromagnetic

$Fe(OH)_2$ - 34 T_N - planar antiferromagnetic

Wüstite - 203-211 T_N - antiferromagnetic

About Verwey transition, see:

https://www.esrf.fr/UsersAndScience/Publications/Highlights/2006/MAT/MAT02

"Magnetite (Fe_3O_4) is a fascinating natural mineral which is a metallic ferrimagnet at ambient conditions. … Magnetite has become an important ingredient in the formation of metallic/magnetic nano-composites. In 1939 Verwey discovered a remarkable phenomenon in magnetite, a discontinuous drop in the conductance on cooling the sample below 122 K. This temperature T_V has been nicknamed the Verwey temperature and was shown to be dependent on stoichiometry".

Appendix D - Tiwari et al. studies

Since we have seen the works by Tiwari et al. mentioned in relation with carbon, let us remember the subjects or their articles, to show that carbon does not exist in them.

In "Probing antiphase boundaries in Fe_3O_4 thin films using micro-Raman spectroscopy", Tiwari and coworkers present a Raman study of magnetite films possessing different thicknesses "grown on single crystal Si and MgO substrates to investigate the presence of antiphase boundaries (APBs). "Raman scattering was performed at room temperature to investigate the effect of substrate and thickness on the vibrational properties. The presence of various modes in Fe_3O_4 can be found in Ref. [Gasparov et al., 2000]. Figure 2 shows the Raman spectra of all the Fe3O4 films" (Tiwari et al.).

In the "Oriented growth of Fe_3O_4 thin film on crystalline and amorphous substrates by pulsed laser deposition", Tiwari and coworkers "have deposited magnetite thin films … from a α-Fe_2O_3 target on different substrates (Si (1 1 1), GaAs (1 0 0), Al_2O_3 (0 0 1) and amorphous float glass (FG)) without any buffer layer at a substrate temperature of 450 °C" (Tiwari et al.).

"The Raman spectra were recorded at room temperature in backscattering configuration using a HR800 Jobin-Yvon spectrometer having a resolution of 1 cm^{-1}. An He–Ne laser (632.8 nm) was used as an excitation source at a power of 9 mW on the sample" (Tiwari et al.).

References

[1] Aisida, S. O., Akpa, P. A., Ahmad, I., Zhao, T. K., Maaza, M., & Ezema, F. I. (2020). Bio-inspired encapsulation and functionalization of iron oxide nanoparticles for biomedical applications. European polymer journal, 122, 109371.

[2] Anthony, J. W., Bideaux, R. A., Bladh, K. W., & Nichols, M. C. (2001). Handbook of mineralogy. Mineral Data Publishing.

[3] Avloni, J., Ouyang, M., Florio, L., Henn, A. R., & Sparavigna, A. (2007). Shielding effectiveness evaluation of metallized and polypyrrole-coated fabrics. Journal of Thermoplastic Composite Materials, 20(3), 241-254.

[4] Bagherzadeh, M., Aslibeiki, B., & Arsalani, N. (2023). Preparation of Fe3O4/vine shoots derived activated carbon nanocomposite for improved removal of Cr (VI) from aqueous solutions. Scientific Reports, 13(1), 3960.

[5] Baghshahi, S., & Yousefi, F. (2021). A New Systematic Approach to the Morphology and Magnetic Properties of Spherical, Cubic, and Rod-like Magnetite Nanoparticles. Journal of Superconductivity and Novel Magnetism, 34, 1949-1954.

[6] Bahari, A. (2017). Characteristics of Fe3O4, α-Fe2O3, and γ-Fe2O3 nanoparticles as suitable candidates in the field of nanomedicine. Journal of Superconductivity and Novel Magnetism, 30, 2165-2174.

[7] Beattie, I. R., & Gilson, T. R. (1970). The single-crystal Raman spectra of nearly opaque materials. Iron (III) oxide and chromium (III) oxide. Journal of the Chemical Society A: Inorganic, Physical, Theoretical, 980-986.

[8] Bersani, D., Lottici, P. P., & Montenero, A. (1999). Micro-Raman investigation of iron oxide films and powders produced by sol–gel syntheses. Journal of Raman spectroscopy, 30(5), 355-360.

[9] Blaney, L. (2007). Magnetite (Fe3O4): Properties, synthesis, and applications. Lehigh Preserve Collection, Volume 15, Paper 5. http://preserve.lehigh.edu/cas-lehighreview-vol-15/5

[10] Boucherit, N., Hugot-Le Goff, A., & Joiret, S. (1991). Raman studies of corrosion films grown on Fe and Fe-6Mo in pitting conditions. Corrosion Science, 32(5-6), 497-507.

[11] Bruschi, M. L., & de Toledo, L. D. A. S. (2019). Pharmaceutical applications of iron-oxide magnetic nanoparticles. Magnetochemistry, 5(3), 50.

[12] Buzgar N., Apopei A. I., & Buzatu A. (2009). Romanian Database of Raman Spectroscopy (http://rdrs.ro).

[13] Chamritski, I., & Burns, G. (2005). Infrared-and Raman-active phonons of magnetite, maghemite, and hematite: a computer simulation and spectroscopic study. The Journal of Physical Chemistry B, 109(11), 4965-4968.

[14] Chen, T., Cai, J., Gong, D., Liu, C., Liu, P., Cheng, X., & Zhang, D. (2023). Facile fabrication of 3D biochar absorbers dual-loaded with Fe3O4 nanoparticles for enhanced microwave absorption. Journal of Alloys and Compounds, 935, 168085.

[15] Cheng, D., Li, X., Zhang, G., & Shi, H. (2014). Morphological effect of oscillating magnetic nanoparticles in killing tumor cells. Nanoscale research letters, 9, 1-8.

[16] Chourpa, I., Douziech-Eyrolles, L., Ngaboni-Okassa, L., Fouquenet, J. F., Cohen-Jonathan, S., Soucé, M., Marchais. H., & Dubois, P. (2005). Molecular composition of iron oxide nanoparticles, precursors

for magnetic drug targeting, as characterized by confocal Raman microspectroscopy. Analyst, 130(10), 1395-1403.
[17] Colombo, M., Carregal-Romero, S., Casula, M.F., Gutiérrez, L., Morales, M.P., Böhm, I.B., Heverhagen, J.T., Prosperi, D., & Parak, W.J. (2012). Biological applications of magnetic nanoparticles. Chemical Society Reviews, 41(11), 4306-4334.
[18] Cornell, R. M., & Schwertmann, U. (2003). The iron oxides: structure, properties, reactions, occurrences, and uses (Vol. 664). Weinheim: Wiley-vch.
[19] Dar, M. I., & Shivashankar, S. A. (2014). Single crystalline magnetite, maghemite, and hematite nanoparticles with rich coercivity. RSC Advances, 4(8), 4105-4113.
[20] De Faria, D. L., Venâncio Silva, S., & De Oliveira, M. T. (1997). Raman microspectroscopy of some iron oxides and oxyhydroxides. Journal of Raman spectroscopy, 28(11), 873-878.
[21] De Jesús Ruíz-Baltazar, Á., Reyes-López, S. Y., de Lourdes Mondragón-Sánchez, M., Robles-Cortés, A. I., & Pérez, R. (2019). Eco-friendly synthesis of Fe3O4 nanoparticles: evaluation of their catalytic activity in methylene blue degradation by kinetic adsorption models. Results in Physics, 12, 989-995.
[22] Degiorgi, L., Blatter-Mörke, I., & Wachter, P. (1987). Magnetite: Phonon modes and the Verwey transition. Physical Review B, 35(11), 5421.
[23] Dünnwald, J., & Otto, A. (1989). An investigation of phase transitions in rust layers using Raman spectroscopy. Corrosion science, 29(9), 1167-1176.
[24] El Mendili, Y., Bardeau, J. F., Randrianantoandro, N., Grasset, F., & Greneche, J. M. (2012). Insights into the mechanism related to the phase transition from γ-Fe2O3 to α-Fe2O3 nanoparticles induced by thermal treatment and laser irradiation. The Journal of Physical Chemistry C, 116(44), 23785-23792.
[25] El Mendili, Y., Abdelouas, A., Ait Chaou, A., Bardeau, Jf., & Schlegel, Ml (2014). Carbon steel corrosion in clay-rich environment. Corrosion Science, 2014, 88, 56-65
[26] El Mendili, Y. (2017). Raman spectrum of goethite from granite SOLSA sample. Personal communication to ROD, 2017
[27] El Mendili, Y., Vaitkus, A., Merkys, A., Gražulis, S., Chateigner, D., Mathevet, F., Gascoin, S., Petit, S., Bardeau, J.-F., Zanatta, M., Secchi, M., Mariotto, G., Kumar, A., Cassetta, M., Lutterotti, L., Borovin, E., Orberger, B., Simon, P., Hehlen, B., & Le Guen, M. (2019). Raman Open Database: first interconnected Raman–X-ray diffraction open-access resource for material identification. Journal of Applied Crystallography, 52(3), 618-625. doi: 10.1107/s1600576719004229
[28] Everall, N. J., Lumsdon, J., & Christopher, D. J. (1991). The effect of laser-induced heating upon the vibrational Raman spectra of graphites and carbon fibres. Carbon, 29(2), 133-137.
[29] Fernández-Remolar, D. C. (2015). Iron Oxides, Hydroxides and Oxy-hydroxides. Encyclopedia of Astrobiology, 1268–1270. https://doi.org/10.1007/978-3-662-44185-5_1714
[30] Fortin, J. P., Wilhelm, C., Servais, J., Ménager, C., Bacri, J. C., & Gazeau, F. (2007). Size-sorted anionic iron oxide nanomagnets as colloidal mediators for magnetic hyperthermia. Journal of the american chemical society, 129(9), 2628-2635.
[31] Gasparov, L. V., Tanner, D. B., Romero, D. B., Berger, H., Margaritondo, G., & Forro, L. (2000). Infrared and Raman studies of the Verwey transition in magnetite. Physical Review B, 62(12), 7939.
[32] Gong, X., Liu, Q., Zhao, W., Lu, Z., & Zhang, T. (2022). Almond C/FexOy composite material based on biomass porous carbon structure with high-efficiency microwave absorbing properties. Journal of Materials Science: Materials in Electronics, 33(16), 13166-13179.
[33] Graves, P. R., Johnston, C., & Campaniello, J. J. (1988). Raman scattering in spinel structure ferrites. Materials Research Bulletin, 23(11), 1651-1660.
[34] Gupta, R., Sood, A. K., Metcalf, P., & Honig, J. M. (2002). Raman study of stoichiometric and Zn-doped Fe3O4. Physical Review B, 65(10), 104430.
[35] Hai, N. H., Phu, N. D., Luong, N. H., Chau, N., Chinh, H. D., Hoang, L. H., & Leslie-Pelecky, D. L. (2008). Mechanism for sustainable magnetic nanoparticles under ambient conditions. Journal -Korean Physical Society, 52(5), 1327.
[36] Han, D. H., Wang, J. P., & Luo, H. L. (1994). Crystallite size effect on saturation magnetization of fine ferrimagnetic particles. Journal of Magnetism and Magnetic Materials, 136(1-2), 176-182.

[37] Hanel, R., Thurner, S., & Tsallis, C. (2009). Limit distributions of scale-invariant probabilistic models of correlated random variables with the q-Gaussian as an explicit example. The European Physical Journal B, 72(2), 263.
[38] Hanesch, M. (2009). Raman spectroscopy of iron oxides and (oxy) hydroxides at low laser power and possible applications in environmental magnetic studies. Geophysical Journal International, 177(3), 941-948.
[39] Hart, T.R., Adams, S.B., Temkin, H. (1976). In: M. Balkanski, R. Leite, S. Porto (Eds.),. Proceedings of the 3rd International. Conference on Light Scattering in Solids, Flammarion, Paris, 1976, pp. 254–258.
[40] He, D., Xiong, Y., Wang, L., Sun, W., Liu, R., & Yue, T. (2020). Arsenic (III) removal from a high-concentration arsenic (III) solution by forming ferric arsenite on red mud surface. Minerals, 10(7), 583.
[41] Hou, Y., Yu, J., & Gao, S. (2003). Solvothermal reduction synthesis and characterization of superparamagnetic magnetite nanoparticles. Journal of Materials Chemistry, 13(8), 1983-1987.
[42] Jacintho, G. V., Corio, P., & Rubim, J. C. (2007). Surface-enhanced Raman spectra of magnetic nanoparticles adsorbed on a silver electrode. Journal of Electroanalytical Chemistry, 603(1), 27-34.
[43] Jacintho, G. V., Brolo, A. G., Corio, P., Suarez, P. A., & Rubim, J. C. (2009). Structural investigation of MFe2O4 (M= Fe, Co) magnetic fluids. The journal of physical chemistry C, 113(18), 7684-7691.
[44] Kiely, C. H. (2006). Materials for nanotechnology notes.
[45] Kozlenko, D. P., Dubrovinsky, L. S., Kichanov, S. E., Lukin, E. V., Cerantola, V., Chumakov, A. I., & Savenko, B. N. (2019). Magnetic and electronic properties of magnetite across the high pressure anomaly. Scientific Reports, 9(1), 4464.
[46] Kumar, P., Tomar, V., Kumar, D., Joshi, R. K., & Nemiwal, M. (2022). Magnetically active iron oxide nanoparticles for catalysis of organic transformations: A review. Tetrahedron, 106, 132641.
[47] Kumar, A., Zanatta, M., Bersani, D., Daldosso, N., & Mariotto, G. (2019). Raman spectrum of Fe3O4. Personal communication to ROD, 2019
[48] Kumar, A.; Zanatta, M.; Bersani, D; Daldosso, N.; Mariotto, G. Raman spectrum of FeHO2. Personal communication to ROD, 2019
[49] Kumar, A.; Zanatta, M.; Bersani, D; Daldosso, N.; Mariotto, G. Raman spectrum of FeO(OH) Personal communication to ROD, 2019
[50] Kumar, R., Sharma, A., Pandey, A., Chaudhary, A., Dwivedi, N., Shafeeq M, M., Mondal, D. P., & Srivastava, A. K. (2020). Lightweight carbon-red mud hybrid foam toward fire-resistant and efficient shield against electromagnetic interference. Scientific Reports, 10(1), 9913.
[51] Lafuente, B., Downs, R. T., Yang, H., & Stone, N. (2015). 1. The power of databases: The RRUFF project. In Highlights in mineralogical crystallography (pp. 1-30). De Gruyter (O).
[52] Lee, S. H., Lee, I., & Roh, Y. (2003). Biomineralization of a poorly crystalline Fe (III) oxide, akaganeite, by an anaerobic Fe (III)-reducing bacterium (Shewanella alga) isolated from marine environment. Geosciences Journal, 7, 217-226.
[53] Lee, J. B., Kim, H. J., Lužnik, J., Jelen, A., Pajić, D., Wencka, M., Jagličić, Z., Meden, A., & Dolinšek, J. (2014). Synthesis and magnetic properties of hematite particles in a" nanomedusa" morphology. Journal of Nanomaterials, 2014, 191-191.
[54] Legodi, M. A., & de Waal, D. (2007). The preparation of magnetite, goethite, hematite and maghemite of pigment quality from mill scale iron waste. Dyes and pigments, 74(1), 161-168.
[55] Lemaire, B. J., Davidson, P., Ferré, J., Jamet, J. P., Petermann, D., Panine, P., Dozov, I., Stoenescu, D., & Jolivet, J. P. (2005). The complex phase behaviour of suspensions of goethite (α-FeOOH) nanorods in a magnetic field. Faraday discussions, 128, 271-283.
[56] Lemaire, B. J., Davidson, P., Petermann, D., Panine, P., Dozov, I., Stoenescu, D., & Jolivet, J. P. (2004). Physical properties of aqueous suspensions of goethite (α-FeOOH) nanorods: Part II: In the nematic phase. The European Physical Journal E, 13(3), 309-319.
[57] Li, J. M., Huan, A. C. H., Wang, L., Du, Y. W., & Feng, D. (2000). Interface effects on magnetoresistance and magnetic-field-reduced Raman scattering in magnetite. Physical Review B, 61(10), 6876.
[58] Li, W., Lv, B., Wang, L., Li, G., & Xu, Y. (2014). Fabrication of Fe 3 O 4@ C core–shell nanotubes and their application as a lightweight microwave absorbent. RSC Advances, 4(99), 55738-55744.

[59] Li, T., Bai, X., Qi, Y. X., Lun, N., & Bai, Y. J. (2016). Fe3O4 nanoparticles decorated on the biochar derived from pomelo pericarp as excellent anode materials for Li-ion batteries. Electrochimica Acta, 222, 1562-1568.
[60] Liu, W., Yang, J., & Xiao, B. (2009). Application of Bayer red mud for iron recovery and building material production from alumosilicate residues. Journal of hazardous materials, 161(1), 474-478.
[61] Mansour, H., Letifi, H., Bargougui, R., De Almeida-Didry, S., Negulescu, B., Autret-Lambert, C., Gadri. A., & Ammar, S. (2017). Structural, optical, magnetic and electrical properties of hematite (α-Fe2O3) nanoparticles synthesized by two methods: polyol and precipitation. Applied Physics A, 123, 1-10.
[62] Martina, M. R., Zoli, L., & Sani, E. (2022). Synthesis and characterization of goethite (α-FeOOH) magnetic nanofluids. International Journal of Thermofluids, 15, 100169.
[63] Meier, R. J. (2005). On art and science in curve-fitting vibrational spectra. Vibrational spectroscopy, 2(39), 266-269
[64] Mishra, A. K., & Ramaprabhu, S. (2011). Nano magnetite decorated multiwalled carbon nanotubes: a robust nanomaterial for enhanced carbon dioxide adsorption. Energy & Environmental Science, 4(3), 889-895.
[65] Mohammed, S., Elnoor, M., & Hamad, I. (2018). The Structural Properties of Iron Oxides using Raman Spectroscopy. J. Sci. Eng. Res., 5, 183-187.
[66] Mücke, A., & Cabral, A. R. (2005). Redox and nonredox reactions of magnetite and hematite in rocks. Geochemistry, 65(3), 271-278.
[67] Murugappan, K., Silvester, D. S., Chaudhary, D., & Arrigan, D. W. (2014). Electrochemical Characterization of an Oleyl-coated Magnetite Nanoparticle-Modified Electrode. ChemElectroChem, 1(7), 1211-1218.
[68] Naudts, J. (2009). The q-exponential family in statistical physics. Central European Journal of Physics, 7, 405-413.
[69] Nauer, G., Strecha, P., Brinda-Konopik, N., & Liptay, G. (1985). Spectroscopic and thermoanalytical characterization of standard substances for the identification of reaction products on iron electrodes. Journal of Thermal Analysis and Calorimetry, 30(4), 813-830.
[70] Nguyen, V. H., Van, H. T., Nguyen, V. Q., Dam, X. V., Hoang, L. P., & Ha, L. T. (2020). Magnetic Fe3O4 nanoparticle biochar derived from pomelo peel for reactive Red 21 adsorption from aqueous solution. Journal of chemistry, 2020, 1-14.
[71] Nguyen, M. D., Tran, H. V., Xu, S., & Lee, T. R. (2021). Fe3O4 Nanoparticles: Structures, synthesis, magnetic properties, surface functionalization, and emerging applications. Applied Sciences, 11(23), 11301.
[72] Ni, S., Wang, X., Zhou, G., Yang, F., Wang, J., Wang, Q., & He, D. (2009). Hydrothermal synthesis of Fe3O4 nanoparticles and its application in lithium ion battery. Materials Letters, 63(30), 2701-2703.
[73] Oblonsky, L. J., & Devine, T. M. (1995). A surface enhanced Raman spectroscopic study of the passive films formed in borate buffer on iron, nickel, chromium and stainless steel. Corrosion Science, 37(1), 17-41.
[74] Oh, S. J., Cook, D. C., & Townsend, H. E. (1998). Characterization of iron oxides commonly formed as corrosion products on steel. Hyperfine interactions, 112(1-4), 59-66.
[75] Ohtsuka, T., Kubo, K., & Sato, N. (1986). Raman spectroscopy of thin corrosion films on iron at 100 to 150 C in air. Corrosion, 42(8), 476-481.
[76] Oraby, H., Tantawy, H. R., Correa-Duarte, M. A., Darwish, M., Elsaidy, A., Naeem, I., & Senna, M. H. (2022). Tuning Electro-Magnetic Interference Shielding Efficiency of Customized Polyurethane Composite Foams Taking Advantage of rGO/Fe3O4 Hybrid Nanocomposites. Nanomaterials, 12(16), 2805.
[77] Owens, F. J., & Orosz, J. (2006). Effect of nanosizing on lattice and magnon modes of hematite. Solid state communications, 138(2), 95-98.
[78] Palmer, S. J., & Frost, R. L. (2009). Characterisation of bauxite and seawater neutralised bauxite residue using XRD and vibrational spectroscopic techniques. Journal of materials science, 44, 55-63.
[79] Panta, P. C., & Bergmann, C. P. (2015). Raman spectroscopy of iron oxide of nanoparticles (Fe3O4). J. Mater. Sci. Eng, 5(3).
[80] Pereira, M. C., Oliveira, L. C. A., & Murad, E. (2012). Iron oxide catalysts: Fenton and Fentonlike reactions–a review. Clay minerals, 47(3), 285-302.

[81] Ponomar, V. P. (2018). Synthesis and magnetic properties of magnetite prepared by chemical reduction from hematite of various particle sizes. Journal of Alloys and Compounds, 741, 28-34.
[82] Ponomar, V. P., Dudchenko, N. O., & Brik, A. B. (2017). Reduction roasting of hematite to magnetite using carbohydrates. International Journal of Mineral Processing, 164, 21-25.
[83] Pouran, S. R., Raman, A. A. A., & Daud, W. M. A. W. (2014). Review on the application of modified iron oxides as heterogeneous catalysts in Fenton reactions. Journal of Cleaner Production, 64, 24-35.
[84] Rull, F., Martinez-Frias, J., Sansano, A., Medina, J., & Edwards, H. G. M. (2004). Comparative micro-Raman study of the Nakhla and Vaca Muerta meteorites. Journal of Raman Spectroscopy, 35(6), 497-503.
[85] Shebanova, O. N., & Lazor, P. (2003). Raman study of magnetite (Fe3O4): laser-induced thermal effects and oxidation. Journal of Raman spectroscopy, 34(11), 845-852.
[86] Shebanova, O. N., & Lazor, P. (2003). Raman spectroscopic study of magnetite (FeFe2O4): a new assignment for the vibrational spectrum. Journal of Solid State Chemistry, 174(2), 424-430.
[87] Slavov, L., Abrashev, M. V., Merodiiska, T., Gelev, C., Vandenberghe, R. E., Markova-Deneva, I., & Nedkov, I. (2010). Raman spectroscopy investigation of magnetite nanoparticles in ferrofluids. Journal of Magnetism and Magnetic Materials, 322(14), 1904-1911.
[88] Soler, M. A., & Qu, F. (2012). Raman spectroscopy of iron oxide nanoparticles. Raman spectroscopy for nanomaterials characterization, 379-416.
[89] Song, K., Lee, Y., Jo, M. R., Nam, K. M., & Kang, Y. M. (2012). Comprehensive design of carbon-encapsulated Fe3O4 nanocrystals and their lithium storage properties. Nanotechnology, 23(50), 505401.
[90] Sparavigna, A. C. (2022). Entropies and Logarithms. Zenodo. DOI 10.5281/zenodo.7007520
[91] Sparavigna A. C. (2023). Iron Oxide Fe3O4 Nanoparticles for Electromagnetic Shielding. ChemRxiv. Cambridge: Cambridge Open Engage; 2023. https://doi.org/10.26434/chemrxiv-2023-g9bkz-v2
[92] Sparavigna, A. C. (2023). Iron Oxide Fe3O4 Nanoparticles with Intrinsic Conducting Polymers and Biochar to Improve the Electromagnetic Shielding Performance of Light Weight Absorption-Type Materials. International Journal of Sciences, 12(08), 5–23. https://doi.org/10.18483/ijsci.2709
[93] Sparavigna, A. C. (2023). The Catcher in the Water: Magnetic Biochar for the Treatment of Wastewater (April 4, 2023). SSRN. http://dx.doi.org/10.2139/ssrn.4409849
[94] Sparavigna, A. C. (2023). q-Gaussian Tsallis Line Shapes and Raman Spectral Bands. International Journal of Sciences, 12(03), 27-40. http://dx.doi.org/10.18483/ijSci.2671
[95] Sparavigna, A. C. (2023). q-Gaussian Tsallis Functions and Egelstaff-Schofield Spectral Line Shapes. International Journal of Sciences, 12(03), 47-50. http://dx.doi.org/10.18483/ijSci.2673
[96] Sparavigna, A. C. (2023). q-Gaussian Tsallis Line Shapes for Raman Spectroscopy (June 7, 2023). SSRN Electronic Journal. http://dx.doi.org/10.2139/ssrn.4445044
[97] Sparavigna, A. C. (2023). Formamide Raman Spectrum and q-Gaussian Tsallis Lines (June 12, 2023). SSRN Electronic Journal. http://dx.doi.org/10.2139/ssrn.4451881
[98] Sparavigna A. C. (2023). Tsallis q-Gaussian function as fitting lineshape for Graphite Raman bands. ChemRxiv. Cambridge: Cambridge Open Engage, https://doi.org/10.26434/chemrxiv-2023-bwnmw
[99] Sparavigna A. C. (2003). Fitting q-Gaussians onto Anatase TiO2 Raman Bands. ChemRxiv. Cambridge: Cambridge Open Engage, https://doi.org/10.26434/chemrxiv-2023-11vqb
[100] Sparavigna, A. (2023). Q-Gaussians and the SERS Spectral Bands of L-Cysteine and Cysteamine. ChemRxiv. Cambridge: Cambridge Open Engage, https://doi.org/10.26434/chemrxiv-2023-9swp9-v2
[101] Srivastava, M., Ojha, A. K., Chaubey, S., Singh, J., Sharma, P. K., & Pandey, A. C. (2010). Investigation on magnetic properties of α-Fe2O3 nanoparticles synthesized under surfactant-free condition by hydrothermal process. Journal of alloys and compounds, 500(2), 206-210.
[102] Sun, X., Zheng, C., Zhang, F., Yang, Y., Wu, G., Yu, A., & Guan, N. (2009). Size-controlled synthesis of magnetite (Fe3O4) nanoparticles coated with glucose and gluconic acid from a single Fe (III) precursor by a sucrose bifunctional hydrothermal method. The Journal of Physical Chemistry C, 113(36), 16002-16008.
[103] Tamura, K., & Endo, H. (1969). Ferromagnetic properties of amorphous nickel. Physics Letters A, 29(2), 52-53.

[104] Tang, W., Khavarian, M., & Yousefi, A. (2022). Red Mud. In Sustainable Concrete Made with Ashes and Dust from Different Sources: Materials, Properties and Applications, Siddique, Rafat, and Rafik Belarbi, eds. Woodhead Publishing, pages 577-606.
[105] Thibeau, R. J., Brown, C. W., & Heidersbach, R. H. (1978). Raman spectra of possible corrosion products of iron. Applied spectroscopy, 32(6), 532-535.
[106] Thierry, D., Persson, D., Leygraf, C., Boucherit, N., & Hugot-Le Goff, A. (1991). Raman spectroscopy and XPS investigations of anodic corrosion films formed on FeMo alloys in alkaline solutions. Corrosion Science, 32(3), 273-284.
[107] Tiwari, S., Prakash, R., Choudhary, R. J., & Phase, D. M. (2007). Oriented growth of Fe3O4 thin film on crystalline and amorphous substrates by pulsed laser deposition. Journal of Physics D: Applied Physics, 40(16), 4943.
[108] Tiwari, S., Phase, D. M., & Choudhary, R. J. (2008). Probing antiphase boundaries in Fe3O4 thin films using micro-Raman spectroscopy. Applied Physics Letters, 93(23).
[109] Tong, S., Zhu, H., & Bao, G. (2019). Magnetic iron oxide nanoparticles for disease detection and therapy. Materials Today, 31, 86-99.
[110] Tsallis, C. (1988). Possible generalization of Boltzmann-Gibbs statistics. Journal of statistical physics, 52, 479-487.
[111] Umarov, S., Tsallis, C., Steinberg, S. (2008). On a q-Central Limit Theorem Consistent with Nonextensive Statistical Mechanics. Milan J. Math. Birkhauser Verlag. 76: 307–328. doi:10.1007/s00032-008-0087-y. S2CID 55967725.
[112] Varadwaj, K. S. K., Panigrahi, M. K., & Ghose, J. (2004). Effect of capping and particle size on Raman laser-induced degradation of γ-Fe2O3 nanoparticles. Journal of Solid State Chemistry, 177(11), 4286-4292.
[113] Venkateswarlu, S., Kumar, B. N., Prasad, C. H., Venkateswarlu, P., & Jyothi, N. V. V. (2014). Bio-inspired green synthesis of Fe3O4 spherical magnetic nanoparticles using Syzygium cumini seed extract. Physica B: Condensed Matter, 449, 67-71.
[114] Verble, J. L. (1974). Temperature-dependent light-scattering studies of the Verwey transition and electronic disorder in magnetite. Physical Review B, 9(12), 5236.
[115] Verwey, E. (1939). Electronic conduction of magnetite (Fe3O4) and its transition point at low temperatures. Nature, 144(3642), 327-328.
[116] Vignat, C., & Plastino, A. (2009). Why is the detection of q-Gaussian behavior such a common occurrence?. Physica A: Statistical Mechanics and its Applications, 388(5), 601-608.
[117] Vind, J., Malfliet, A., Bonomi, C., Paiste, P., Sajó, I. E., Blanpain, B., Tkaczyk.. A. H., Vicky Vassiliadou, V., & Panias, D. (2018). Modes of occurrences of scandium in Greek bauxite and bauxite residue. Minerals Engineering, 123, 35-48.
[118] Wallyn, J., Anton, N., & Vandamme, T. F. (2019). Synthesis, principles, and properties of magnetite nanoparticles for in vivo imaging applications—A review. Pharmaceutics, 11(11), 601.
[119] Wang, P., & Liu, D. Y. (2012). Physical and chemical properties of sintering red mud and bayer red mud and the implications for beneficial utilization. Materials, 5(10), 1800-1810.
[120] Witkovský, V. (2023). Characteristic Function of the Tsallis q-Gaussian and Its Applications in Measurement and Metrology. Metrology, 3(2), 222-236.
[121] Wu, W., Wu, Z., Yu, T., Jiang, C., & Kim, W. S. (2015). Recent progress on magnetic iron oxide nanoparticles: synthesis, surface functional strategies and biomedical applications. Science and technology of advanced materials, 16(2), 023501.
[122] Wyckoff, R. W. G. (1963). Second edition. Crystal Structures, 1963, 1, 290-295, Interscience Publishers, New York
[123] Xuan, S., Hao, L., Jiang, W., Gong, X., Hu, Y., & Chen, Z. (2007). A facile method to fabricate carbon-encapsulated Fe3O4 core/shell composites. Nanotechnology, 18(3), 035602.
[124] Yew, Y. P., Shameli, K., Miyake, M., Khairudin, N. B. B. A., Mohamad, S. E. B., Hara, H., Bt Mad Nordin, M.F., & Lee, K. X. (2017). An eco-friendly means of biosynthesis of superparamagnetic magnetite nanoparticles via marine polymer. IEEE Transactions on Nanotechnology, 16(6), 1047-1052.
[125] Yuvakkumar, R., & Hong, S. I. (2014). Green synthesis of spinel magnetite iron oxide nanoparticles. Advanced Materials Research, 1051, 39-42.